

Quasar Tomography: Unification of Echo Mapping and Photoionisation Models

Keith Horne¹, Kirk T. Korista², Michael R. Goad³

¹*Physics & Astronomy, St. Andrews University, North Haugh, St. Andrews, KY16 9SS, Scotland, UK. kdh1@st-and.ac.uk.*

²*Department of Physics, Western Michigan University, 1120 Everett Tower, Kalamazoo, MI, 49008, USA. korista@wmich.edu.*

³*Physics & Astronomy, University of Southampton, Southampton SO17 1BJ, UK. mrg@astro.soton.ac.uk.*

Accepted 2002 Sep 4, Submitted 2002 Jul 26

ABSTRACT

Reverberation mapping aims to use time-delayed variations in photoionised emission lines to map the geometry and kinematics of emission-line gas in the vicinity of an active galactic nucleus. By fitting to a time-variable emission line profile, one can reconstruct a 2-dimensional map $\Psi(\tau, v)$, where τ is the time delay and v is the Doppler shift, for each emission line. In this paper we develop quasar tomography, which combines the time delay and velocity information with photoionisation physics in order to map the reprocessing region using information assembled from many different emission lines. The observed spectral variations are modelled in terms of direct light from the active nucleus and time-delayed reprocessed light from surrounding gas clouds. We use the photoionisation code CLOUDY to evaluate line and continuum reprocessing efficiencies $\epsilon(\lambda, \Phi_{\text{H}}, n_{\text{H}}, N_{\text{H}}, \theta)$ for clouds of hydrogen density n_{H} and column density N_{H} exposed to hydrogen-ionising photon flux Φ_{H} . The gas distribution is described by a 5-dimensional map, the differential covering fraction $f(R, \theta, n_{\text{H}}, N_{\text{H}}, v)$, which we reconstruct from the 2-dimensional data $F_{\lambda}(\lambda, t)$ by using maximum entropy techniques. Tests with simulated data and a variety of geometries (shells, rings, disks, clouds, jets) are presented to illustrate some of the capabilities and limitations of the method. Specifically, we reconstruct 3-dimensional geometry-density maps, $f(R, \theta, n_{\text{H}})$, by fitting to well-sampled light curves for the continuum and 7 ultraviolet emission lines. The maps are distorted in ways that we understand and discuss. The most successful test recovers a hollow shell geometry, determining correctly its radius and density. The data constrain the ionisation parameter $U \propto R^{-2} n_{\text{H}}^{-1}$ to about 0.1 dex, the radius R to 0.15 dex, and n_{H} to 0.3 dex. We expect better constraints to arise from future fits using more lines and velocity profiles as well as velocity-integrated line fluxes. The maps are sensitive to the assumed distance, offering some prospects for using emission-line reverberations to measure the luminosities and distances of active galactic nuclei.

Key words: methods: data analysis – techniques: spectroscopic – quasars: emission lines – galaxies: Seyfert – galaxies: active – ultraviolet: galaxies

1 INTRODUCTION

1.1 Photoionisation Modelling

Our understanding of the emission-line spectra of active galactic nuclei (AGNs) has progressed considerably since the late 1970s, when photoionisation calculations were first used to model observed spectra in an effort to determine the physical characteristics of the emission-line gas (e.g., Davidson & Netzer 1979). Sophisticated photoionisation codes now embody our current detailed knowledge and understanding of atomic physics and physical processes in astrophysical plasmas. The evolution of these codes toward increasing realism

is guided by detailed comparison of observed and predicted spectra, made possible by advances in high-speed computing.

In the photoionisation code CLOUDY (Ferland et al. 1998), a prescribed spectrum L_{λ} is directed into a gas cloud at radius R characterized by its hydrogen density n_{H} and hydrogen column density N_{H} . The temperature and ionisation state of the gas in successive zones inside the cloud are evaluated, as well as the line and continuum fluxes that emerge from the front and back faces of the cloud. For given elemental abundances, the calculated emission-line flux ra-

tios depend upon L_λ , R , n_{H} , and N_{H} . However, the primary dependence is upon the ionisation parameter

$$U \equiv \frac{Q_{\text{H}}}{4\pi R^2 n_{\text{H}} c} = \frac{\Phi_{\text{H}}}{n_{\text{H}} c}, \quad (1)$$

where

$$Q_{\text{H}} = \int_0^{\lambda_{\text{H}}} \frac{\lambda L_\lambda d\lambda}{hc} \quad (2)$$

is the rate at which the source emits hydrogen-ionising photons ($\lambda < \lambda_{\text{H}} = 912\text{\AA}$), and

$$\Phi_{\text{H}} = \frac{Q_{\text{H}}}{4\pi R^2} \quad (3)$$

is the flux of hydrogen-ionising photons incident on the cloud. By comparing observed emission-line ratios (which are rather similar for most objects) with predictions from single-cloud photoionisation calculations, “typical” physical conditions in the emission-line gas are inferred to be $n_{\text{H}} \sim 10^{9.5} \text{ cm}^{-3}$, $U \sim 10^{-2}$, $\Phi_{\text{H}} \sim 10^{18} \text{ cm}^{-2} \text{ s}^{-1}$ (Davidson & Netzer 1979). For these parameters the distance of the gas cloud from the nucleus is

$$R = \left(\frac{Q_{\text{H}}}{4\pi \Phi_{\text{H}}} \right)^{1/2} \sim 100 L_{44}^{1/2} \text{ light days}, \quad (4)$$

where $L_{44} \sim Q_{\text{H}} hc/\lambda_{\text{H}}$ is the hydrogen-ionising luminosity of the source in units of $10^{44} \text{ erg s}^{-1}$.

Since the derived gas temperatures are low ($T \sim 10^4 \text{ K}$), the broad emission-line profiles ($V_{\text{FWHM}} \sim 5000 \text{ km s}^{-1}$) are interpreted as arising from bulk motion of the emission-line gas, most likely arising from gravitational acceleration of the gas by the nucleus. A rough virial mass may then be estimated by combining the V_{FWHM} with the radius estimated above,

$$M \sim 4 \times 10^8 M_\odot \left(\frac{V_{\text{FWHM}}}{5000 \text{ km s}^{-1}} \right)^2 \left(\frac{R}{100 \text{ light days}} \right). \quad (5)$$

The rough similarity of observed emission-line ratios in high-luminosity quasars and lower-luminosity Seyfert galaxies suggests that although these active galactic nuclei span a wide range of luminosity, their emission-line regions are nevertheless characterized by roughly the same ionisation parameter. Moreover, in many cases comparison of velocity widths and profiles of different emission lines suggests that U is roughly independent of R and hence $n_{\text{H}} \propto R^{-2}$. These regularities in the observed properties of quasar emission lines have become recognized as a problem because it is not known what mechanisms may regulate conditions in the emission-line gas to ensure a constant ionisation parameter.

A plausible solution to this “fine-tuning” problem has recently emerged. The LOC model (Locally Optimally-emitting Clouds, e.g., Baldwin et al. 1995) proposes that the photoionised gas is not adequately characterized by a single density and column density at each radius, $n_{\text{H}}(R)$, $N_{\text{H}}(R)$. Instead, a whole population of gas clouds, $f(R, n_{\text{H}}, N_{\text{H}})$, provides for a wide range of n_{H} and N_{H} at each R . The total emission in a given line is then obtained by summing contributions from all these different cloud types, but most of the emission arises from the specific cloud types that are maximally efficient in producing that particular line. The photoionisation models indicate that high reprocessing efficiency in a given line is achieved by a sub-population of

the clouds defined primarily by a specific range of ionisation parameter. In the LOC model, the optimal conditions are obtained at many radii in a given source by employing lower density gas when farther from the nucleus, and over a wide range of source luminosity by using gas at larger radius in higher-luminosity sources. Thus the apparent fine tuning is a consequence of photoionisation physics rather than specific conditions in the emission-line gas.

1.2 Reverberation Mapping

The assumption that the emission lines are driven by photoionisation is amply validated by variability monitoring campaigns. The active nuclei in half a dozen Seyfert 1 galaxies have been studied by the AGN Watch collaboration (Alloin et al. 1994), combining *IUE* and ground-based observations to monitor variability in the ultraviolet and optical spectra. The AGN Watch campaigns extend over many months, with time sampling typically a few days (Peterson 1993). In all cases the observed variations in the continuum flux, $F_c(t)$, are accompanied by correlated variations in emission-line fluxes, $F_\ell(t)$. Moreover, the emission line variations lag behind those seen in the continuum. The time delay, τ , can be interpreted as light-travel time. This effectively measures the radial distance,

$$R \sim \frac{c\tau}{(1+z)}, \quad (6)$$

from the nucleus (more accurately from the continuum-emitting regions close to the nucleus) to the line-emitting region. Here z is the cosmological redshift of the source.

The time delays are usually estimated by cross-correlating the observed line and continuum light curves (e.g., Edelson & Krolik 1988, Koratkar & Gaskell 1991, White & Peterson 1994). These results have revealed time delays of days to weeks, with shorter delays in the higher ionisation lines, consistent with more highly ionised gas occurring closer to the nucleus (e.g., Clavel et al. 1991).

More detailed information can be extracted by “reverberation mapping” (Bahcall, Kozlovsky & Salpeter 1972, Blandford & McKee 1982). A delay map $\Psi(\tau)$ can be recovered by fitting to high-quality densely-sampled light curves, for example by using the linear echo model

$$F_\ell(t) = \int_0^{\tau_{\text{max}}} \Psi(\tau) F_c(t - \tau) d\tau. \quad (7)$$

Maximum entropy fitting techniques have proven to be useful in this regard (e.g., Horne, Welsh & Peterson 1991, Krolik et al. 1991, Horne 1994), as have regularized linear inversion methods (Vio, Horne & Wamsteker 1994, Pijpers & Wanders 1994, Krolik & Done 1995).

For the strongest lines, C IV in particular, data quality can be sufficient to record reverberation effects in the velocity profiles, allowing the recovery of kinematic information in the form of a velocity–delay map $\Psi(v, \tau)$ (e.g., Wanders et al. 1995, Ulrich & Horne 1996, Done & Krolik 1996). Results to date show that the red and blue wings of the C IV emission line respond together with smaller delays than the line centre. Models involving purely radial inward or outward motions are ruled out, but a variety of models involving primarily random or azimuthal motions, as in a disk, are permitted.

Time delays measured from $H\beta$ and optical continuum light curves of AGNs with a range of luminosities ($10^{41.8} \text{ erg s}^{-1} < \lambda L_{\lambda}(5100\text{\AA}) < 10^{45.7} \text{ erg s}^{-1}$) establish an empirical relationship of the form

$$R_{H\beta} \sim 30 \left(\frac{\lambda L_{\lambda}(5100\text{\AA})}{10^{44} \text{ erg s}^{-1}} \right)^{0.7} \text{ light days} \quad (8)$$

(Kaspi et al. 2000). This is consistent with the photoionised region increasing in size as the ionising luminosity increases.

The echo-mapping experiments have forced us to realize that emission-line gas is present much closer to the nucleus than the radius estimated in Equation (4) on the basis of single-cloud photoionisation models. For a given U , the smaller radius requires a higher density, $n_{\text{H}} \sim 10^{11} \text{ cm}^{-3}$ (Ferland et al. 1992). In earlier work, the $\text{C III]} / \text{C IV}$ ratio was used to argue against such high densities. This argument may be incorrect, however, if C III] and C IV form in different regions with different densities, as is suggested in several cases where the C III] lag is longer than the C IV lag (Clavel et al. 1991, Reichert et al. 1994). The smaller radii also reduce the inferred virial masses.

1.3 Quasars as Cosmological Probes

Quasars are potentially important as cosmological probes. Their high luminosity renders them visible at large redshifts. However, quasars are poor standard candles, with luminosities ranging over many orders of magnitude. In low-redshift samples the emission-line ratios and equivalent widths are correlated with luminosity (Baldwin 1977; Baldwin et al. 1978; Kinney et al. 1990), but the dispersion is too large to be of much use in estimating luminosities or distances. Separating luminosity and evolution effects is also difficult with magnitude-limited samples that tend to include high-luminosity objects at high redshift and low-luminosity objects at low redshift.

Distances may alternatively be estimated by using light travel time delays from reverberation effects to measure the linear size of something whose angular size can be directly observed or inferred from the observed spectrum. For example, the distance to supernova 1987A was estimated from time-delayed enhancements in photoionised emission lines produced when the ultraviolet flash from the explosion first reached the inclined circumstellar ring that is resolved by HST (Panagia et al. 1991). Can we apply a similar method to AGNs?

For AGNs a method based on reverberations in continuum emission from the irradiated surface of the accretion disc has been demonstrated by Collier et al. (1999). A steady-state disc is predicted to have a characteristic temperature profile of the form $T \propto R^{-3/4}$. With $\tau \sim (1+z)R/c$ from light travel time, and $kT \sim hc(1+z)/4\lambda$ from blackbody radiation, the temperature decreasing with radius implies a time delay increasing with wavelength as $\tau \propto \lambda^{4/3}(1+z)^{-1/3}$. Just such an effect was found, with delays of order 1-2 days between ultraviolet and optical continuum variations in the Seyfert 1 galaxy NGC 7469. The resulting redshift-independent distance yields $H_0 \sqrt{\cos i / 0.7} = 42 \pm 8 \text{ km s}^{-1} \text{ Mpc}^{-1}$, where i is the inclination of the disk axis to the line of sight, expected to be less than 60° for Seyfert 1 galaxies.

In §3 of this paper we discuss a new method of estimating distances to AGNs based on reverberation in the photoionised emission lines. The basic idea is to require the radii of photoionised regions estimated from time delays to match the radii derived from comparison of photoionisation calculations with the observed emission-line ratios. This may provide a new direct method of determining distances, based on a straightforward interpretation of time delays and photoionisation physics.

1.4 Quasar Tomography

The goal of quasar tomography, as developed in this paper, is to unify echo mapping and photoionisation modelling. Echo mapping reveals the sizes of emission-line regions while photoionisation modelling uses emission-line flux ratios to determine physical conditions within the emission-line gas. Current echo mapping techniques define delay maps for each line independently of the other lines and without regard to photoionisation physics. More complete information can be extracted from high-quality time-resolved emission-line spectra by combining these two approaches.

Following the spirit of the LOC model, we offer the emission-line gas freedom to fill out a very general 5-dimensional map, $f(R, \theta, n_{\text{H}}, N_{\text{H}}, v)$, giving the differential covering fraction of the gas clouds. We then expect observations of time-dependent spectra $F_{\lambda}(\lambda, t)$ to reveal the geometry, physical conditions, and kinematics of the gas by placing constraints that define the structure of the 5-D cloud map.

We are aiming to fit simultaneously, in far greater detail than has hitherto been attempted, the time-dependent fluxes and velocity profiles of numerous emission lines recorded in high quality spectra. Our methods and assumptions in modelling the reverberating spectrum $F_{\lambda}(\lambda, t)$ are developed in Appendix A. Appendix B then discusses the maximum entropy techniques we employ to recover the cloud map $f(R, \theta, n_{\text{H}}, N_{\text{H}}, v)$ by fitting to the observations of $F_{\lambda}(\lambda, t)$.

In §2 we illustrate some of the capabilities and limitations of quasar tomography by presenting the results of test reconstructions from simulated datasets. A variety of possible geometries is considered. In §3 we assess prospects for using this approach to derive redshift-independent distances and luminosities. Concluding remarks are made in §4.

2 CLOUD MAPS RECOVERED FROM SIMULATED DATASETS

2.1 Appearance of Different Geometries

It is important to realize that most types of observational data obtained from a distant unresolved object are unaffected if the object is rotated by an angle ϕ around the line of sight. A possible exception is polarimetric data, where the position angle of linearly polarized light is measured. In quasar tomography we employ information from time delays and emission-line ratios that are sensitive to R and θ but not to ϕ . Thus we should not expect to be able to recover the 3-dimensional source geometry, $f(R, \theta, \phi)$, but rather the 2-dimensional geometry,

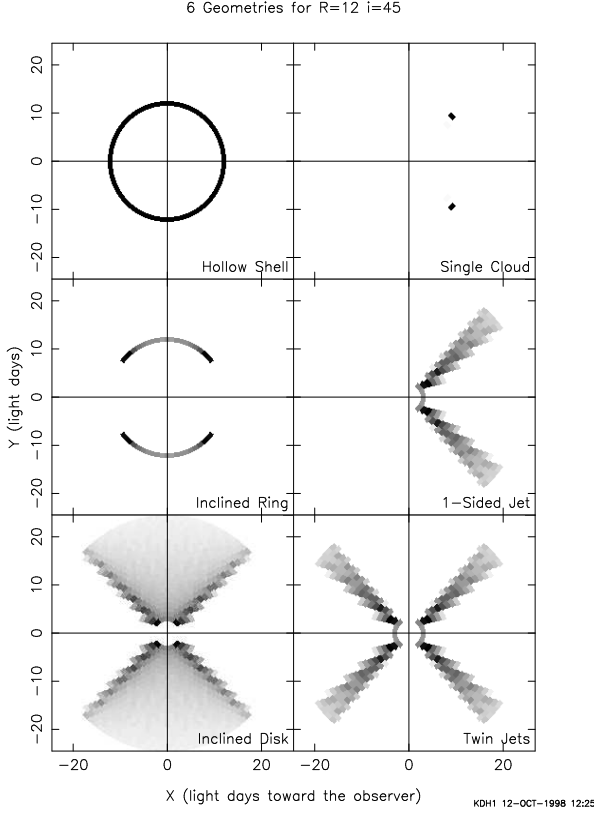


Figure 1. Maps showing the appearance of six different geometries after being rotated around the line of sight (X axis).

$$f(R, \theta) = \int f(R, \theta, \phi) d\phi, \quad (9)$$

that arises by rotating the 3-dimensional geometry around the line of sight to the observer.

To illustrate the effect of this ambiguity, Fig. 1 displays the appearance of several simple geometries after projection around the line of sight onto the X, Y plane. Here $X = -R \cos \theta$ is measured from the nucleus towards the observer, whose location is off to the right-hand side of the figure, and $Y = R \sin \theta$ is measured perpendicular to the line of sight. The ambiguity in ϕ means that we can project any given geometry by rotating it around the line of sight. This yields a projected 2-dimensional geometry that is symmetric to reflection through the X axis. A single cloud (upper-right panel) projects to a spot at the appropriate radius R and azimuth θ , plus its mirror image reflected through the X axis. A hollow spherical shell (upper-left panel) projects to a complete ring with radius R equal to that of the shell.

An inclined ring or annulus (middle-left panel) projects to an arc of radius R that straddles the $+Y$ axis, plus its mirror image on the $-Y$ axis. The arc spans $\theta = 90^\circ \pm i$, where i is the inclination angle between the ring axis and the line of sight. The figure shows the projection of a ring inclined by $i = 45^\circ$. If we tilt the ring axis toward the observer, the two arcs become shorter, shrinking to a pair of spots at $Y = \pm R$ as $i \rightarrow 0$. Tilting the ring axis away from the observer makes the arcs longer until their endpoints meet to form a complete ring as $i \rightarrow 90^\circ$. This edge-on ring may still be distinguished from the hollow shell, however, because a

relatively large fraction of the ring’s circumference projects to the region near the endpoints of the arc.

An inclined disk (lower-left panel) is assembled from a set of co-axial annuli with different radii. The disk annuli project to arcs of different radii that fill out the sector bounded by the smallest and largest arcs. This makes an X-shaped pattern with the sectors above and below the X filled in and empty sectors to the sides. As with the inclined ring, tilting the disk toward (away from) the line of sight closes (opens) the filled sector of the X.

A 1-sided hollow conical jet (middle-right panel) is easily recognizable from its projection to a cone emerging from the nucleus. The jet inclination i is the angle between the cone and the X axis, and the jet opening angle ω is the same as that of the cone. Of course the mirror image of the jet, projected across the X axis, is also present after rotation about the line of sight. If we increase the jet opening angle, the corresponding cone becomes wider, eventually overlapping with its mirror image when $\omega > i$. Finally, twin jets extending in opposite directions (lower-right panel) project to an X-shaped pattern of cones.

The main point we wish to make here is that these six geometries, and many others, have distinct appearances after projection by rotation around the line of sight onto the $X - Y$ plane that we aim to recover from the data. In §2.3 we present and discuss maps of these same six geometries reconstructed from simulated datasets.

2.2 Synthetic Light Curves

Fig. 2 shows a simulated dataset calculated using the methods outlined in Appendix A for the geometrically-thin spherical shell shown in Fig 1. All clouds within the shell are assumed to have a gas hydrogen density of $n_{\text{H}} = 10^{11} \text{ cm}^{-3}$, and a hydrogen column density of $N_{\text{H}} = 10^{23} \text{ cm}^{-2}$.

The bottom panel shows the driving light curve, $F_c(t)$, and the responding emission-line light curves $F_\ell(t)$ are shown for 7 different ultraviolet emission lines in the 7 panels above. The data points in these panels were generated by first evaluating the true light curve, and then adding a Gaussian random variate with zero mean and standard deviation as shown by the vertical error bars (smaller than the data points plotted) to simulate 3% observational errors. The horizontal dashed lines show the background fluxes $F_B(\lambda)$ for each line, included in the model to represent constant line emission that is not driven by photoionisation. Light curves similar to these would be possible to obtain in one year of observation by observing once every two days.

Delay maps $\Psi_\ell(\tau)$ are shown in Fig. 2 to the left of the corresponding light curve for each emission line ℓ . The delay maps for this geometrically-thin spherical shell with $R = 12$ light days extend from 0 to $2R/c = 24$ light days. The prompt response (at $\tau = 0$) arises from the near edge of the shell, while the response with maximum delay ($\tau = 2R(1+z)/c$) arises from the far edge of the shell. When the line emission is isotropic (e.g., C III] in Fig. 2) then the delay map for the spherical shell is flat-topped, with equal response in each interval of τ from 0 to $2R(1+z)/c$. For the other lines the delay maps have a positive slope (response increasing with increasing τ) due to their inward anisotropy (enhanced emission at large delays arising from the far edge of the shell).

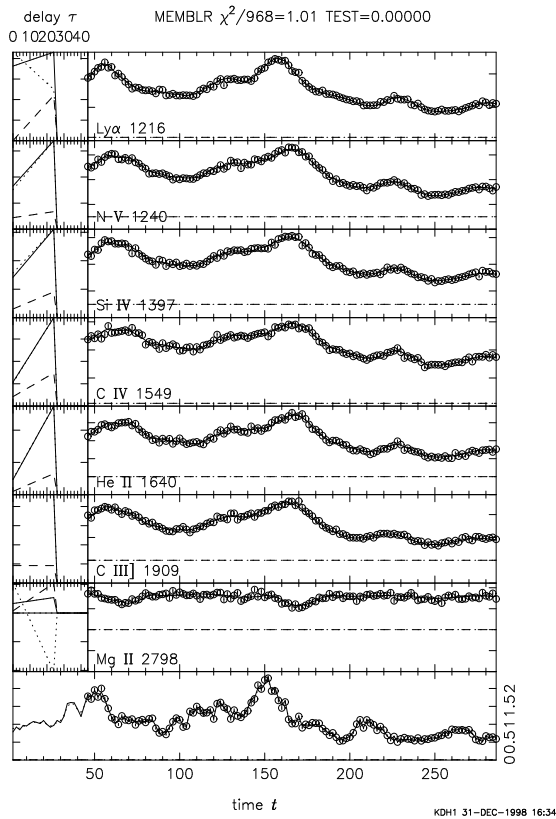


Figure 2. Simulated continuum and emission-line light curves for a thin spherical shell. The continuum light curve (lower panel) convolved with the appropriate delay map (left panels) gives the corresponding emission-line light curve (right panels). The delay maps account for light travel time delays as well as non-linear and anisotropic emission-line responses to variations in the ionising radiation. See text §2.2 for details.

The exact angular pattern of anisotropic line radiation depends of course on details of geometry and radiative transfer in the reprocessing region. These details are beyond the scope of current 1-dimensional photoionisation codes. We are therefore handling the anisotropic line emission by using CLOUDY to evaluate the inward and outward emission of the line, and then interpolating linearly in $\cos\theta$ to obtain the emissivity in direction θ . For further discussion see §A4.1.

The driving light curve (bottom panel of Fig. 2) varies by a factor ~ 4 in this example, and the delay maps can change appreciably when the ionising flux changes by such a large factor between the bright and faint states. To illustrate this, the left panels of Fig. 2 give delay maps corresponding to both the bright state (solid curves) and the faint state (dashed curves) corresponding to the maximum and minimum of the driving light curve. A third delay map (dotted curve) is the difference between the bright and faint state delay maps, scaled to have the same peak as the bright state map. This presentation makes it easy to spot non-linear line responses. The scaled difference map (dotted curve) will differ from the bright state map (solid curve) only if there is a significant non-linear response in that emission line. It can be seen that the responses in all lines are positive and essentially linear, with the exceptions of Ly α , and Mg II.

Ly α shows a marked non-linear response primarily due to a change in the line radiation pattern between the faint and bright states. In the faint state, Ly α has a strong inward anisotropy because its large optical depth causes the bulk of its emission to emerge from the irradiated faces of clouds (Ferland et al. 1992; O’Brien et al. 1994). Thus we see stronger Ly α emission from clouds on the far side of the shell than we do from those on the near side. In contrast, Ly α emission is almost isotropic in the bright state because the hydrogen-ionisation front pushes through the clouds, so that those on the near side of the shell become visible. Thus in the top left panel of Fig. 2 we see that in the low state (dashed delay map) the prompt Ly α response at $\tau = 0$, arising from the near side of the shell, is essentially zero. In the high state (solid delay map), the Ly α response is almost independent of τ , indicating nearly isotropic Ly α emission from the spherical shell.

The Mg II response is also non-linear. Moreover, the Mg II response on the far side of the shell is negative, meaning that Mg II emission decreases with increasing ionising flux. In the faint state, the Mg II radiation is dominated by emission from the irradiated sides of the clouds, producing a strong inward anisotropy with very low prompt response. In the bright state, the Mg II emitting zone becomes significantly depleted as the hydrogen-ionisation front moves deeper into the cloud, and the line emerges more isotropically. The depletion of the partially ionised zone where this line is formed results in a net negative response for this line (see also Goad et al. 1993; O’Brien et al. 1995). The negative response of Mg II can be seen directly in the light curves, where the Mg II flux has minima at times when the other line fluxes have maxima.

In the spherical shell example we are considering, diagnosis of the delay maps reveals isotropic and anisotropic emission, linear and non-linear responses, and positive and negative responses in the various emission lines. Each of these effects conveys information about the possible location and physical state of the gas clouds that are responding to changes in the flux of ionising radiation represented in the dataset by the driving light curve. The information we seek is not readily available, however, as it appears in the delay maps rather than in the observed light curves. We must therefore consider to what extent it is possible to recover the geometry and physical conditions by fitting to the light curves.

2.3 Fits to Synthetic Light Curves

Fig. 3 shows our fit to the simulated dataset of Fig. 2. This fit is accomplished, using the maximum entropy methods discussed in Appendix B, by adjusting the driving light curve $L(t)$, the background spectrum $F_B(\lambda)$, and the cloud geometry and density map $f(R, \theta, n_H)$. We hold the column density fixed at the correct value $N_H = 10^{23} \text{ cm}^{-2}$. Note that our model does not assume a spherical shell geometry with all clouds having the same density, but rather determines what geometry and density distribution are required in order to fit the light curves.

The predicted light curves are required to achieve a good fit, as judged by the criterion $\chi^2/N = 1$, where $N = 968$ is the number of data points. The fitted model predicts line fluxes that are not quite as high as the data

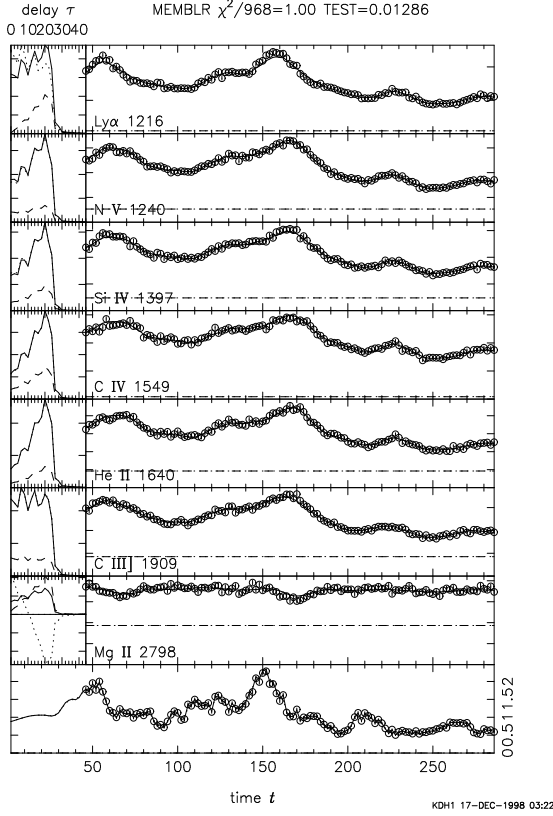


Figure 3. A fit to simulated continuum and emission-line light curves for a thin spherical shell. See text §2.3 for details.

in the peaks of the light curve, particularly for Ly α . This is the principal defect in the fit. It arises because our maximum entropy fit seeks the “smoothest” functions that fit the data points. The reconstructed delay maps, $\Psi_\ell(\tau)$, are noisy at the 10% level, but they do bear a satisfying resemblance to the true delay maps shown in Fig. 2.

The maximum entropy fitting techniques are discussed in detail in Appendix B, but it may be appropriate here to summarise the method and discuss a few issues. The fit arises by iterating from initial guesses for the driving light curve $L(t)$, the background spectrum $F_B(\lambda)$, and the cloud map $f(R, \theta, n_H)$. The iteration seeks to improve the fit to the data, aiming for $\chi^2/N = 1$, while also maximizing the “entropy” to keep the model “as simple as possible”, in a well defined sense. The iteration either converges or else informs you that it has failed to converge. The converged model represents the “simplest” model that fits the data with $\chi^2/N = 1$.

The maximum entropy fit is unique in the sense that it does *not* depend on the initial guesses, and can be reached from a wide range of starting points. However, in a different sense the maximum entropy fit is not unique because there are a variety of ways to define what you mean by “as simple as possible”. For the fits presented in this section, we follow our usual practice of defining “simple” to mean “smooth”. Maximizing the entropy “steers” each parameter of the model toward values in adjacent pixels. This delivers the “smoothest” background spectrum, driving light curve, and cloud map that succeed in fitting the data. When two

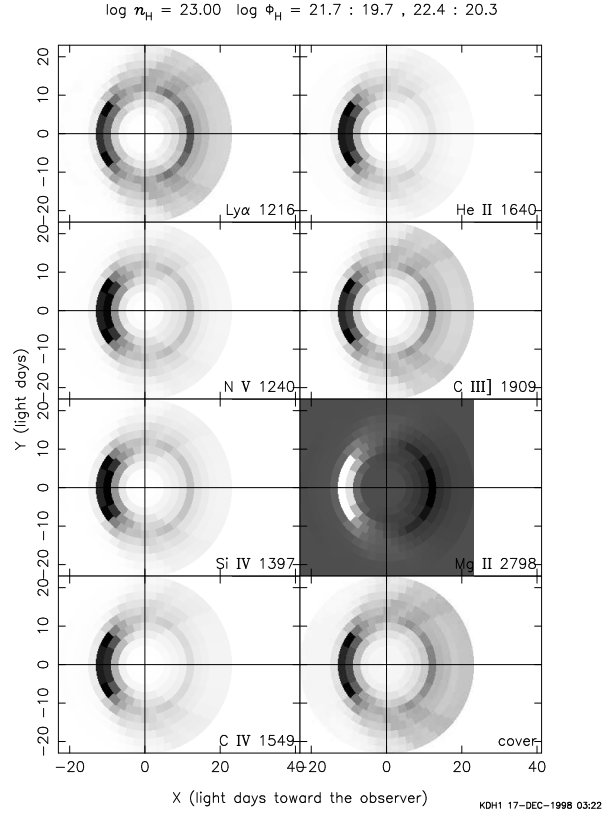


Figure 4. Maps derived from a maximum entropy fit to the simulated data shown in Fig. 3. The reconstructed geometry $f(R, \theta)$, shown in the lower-right panel, reveals the basic form of a hollow spherical shell, with some smearing along the iso-delay parabolas, $\tau \propto R(1 + \cos \theta)$, opening to the right. The other panels display maps of the responses of different emission lines to increases in ionising radiation from the central source. The greyscale assigns white and black to the minimum and maximum responses occurring in each line. Positive responses are exhibited by all lines except Mg II, which has a negative response on the far side and a positive response on the near side of the shell. See text §2.3.1 for further discussion.

models fit the data equally well, the smoother model is preferred. When the data require a sharp feature in the map, e.g. a peak in the spectrum or light curve, or clouds concentrated at some radius or with some density, maximizing entropy spreads out the feature as much as possible in any directions permitted by the data. In this way the resolution of the map is determined by the quality of the data, and the sensitivity of the data to each part of the map. We will point out examples of this effect below.

2.3.1 Density–Geometry Maps of the Spherical Shell

Our maximum entropy fit to the light curves in Fig. 3 recovers a 3-dimensional map, $f(R, \theta, n_H)$, specifying the geometry and density distribution of the emission-line clouds. We visualize this by displaying 2-dimensional projections, $f(R, \theta)$ in Fig. 4 and $f(R, n_H)$ in Fig. 5, which we discuss below.

Fig. 4 shows the reconstructed geometry. The lower-right panel gives the differential covering fraction, $f(R, \theta)$,

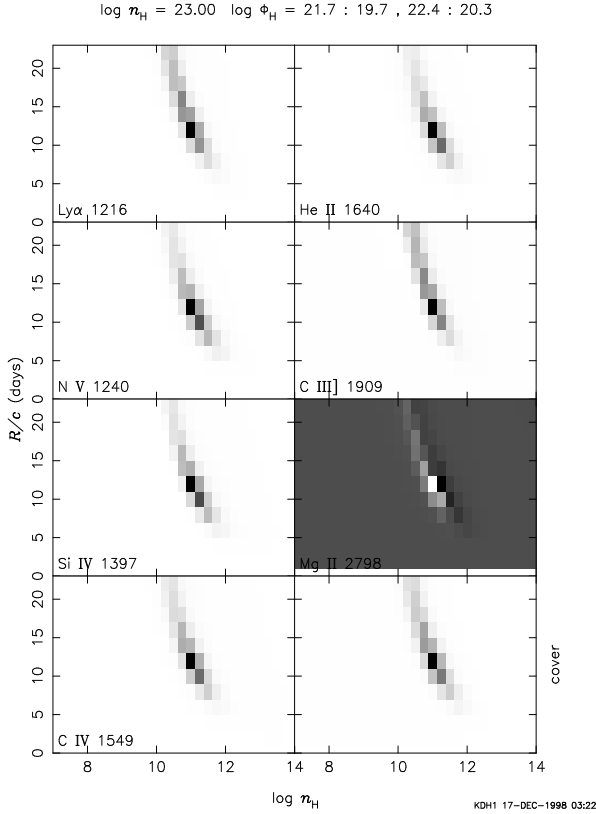


Figure 5. The density-radius map $f(R, n_H)$ recovered from the fit to the simulated data shown in Fig. 3. The correct density $n_H = 10^{11} \text{ cm}^{-3}$ is recovered, with ambiguity along the direction of constant ionisation parameter $U \propto R^{-2} n_H^{-1}$.

and the other panels show the responses in the seven ultra-violet emission lines. The basic morphology of a thin spherical shell, with radius $R/c \sim 12$ light days, is clearly recognizable, though distorted in ways that we understand and discuss below. The inward anisotropy in most of the lines (stronger response from the far side of the shell) is recovered. Mg II looks peculiar in the plot because clouds on the far side of the shell have a negative response in this line. A hollow inner region, $R \lesssim 10$ light days, is clearly recovered. On the far side of the shell, the cloud distribution is confined to within $\lesssim 2$ light days of the correct radius. At other azimuths, however, the clouds have spread outward along iso-delay parabolas, which open toward the right. Striations along the iso-delay parabolas are visible mainly at the top and bottom of the shell.

Fig. 5 shows the density-radius projection, $f(R, n_H)$. Here we see that the correct density, $n \sim 10^{11} \text{ cm}^{-3}$, is recovered, though with smearing along the direction of constant ionisation parameter, $U \propto R^{-2} n_H^{-1}$. The line ratios evidently constrain U to within about 0.1 dex, while the constraints on n_H and hence R are weaker, 0.3 and 0.15 dex respectively. The data allow clouds can move to a larger (smaller) R provided they reduce (increase) n_H to maintain a fixed ionisation parameter, i.e. $n_H \propto R^{-2}$. The line ratios constrain n_H because each emission line becomes optically thin, due to thermalisation or de-excitation, above a different crit-

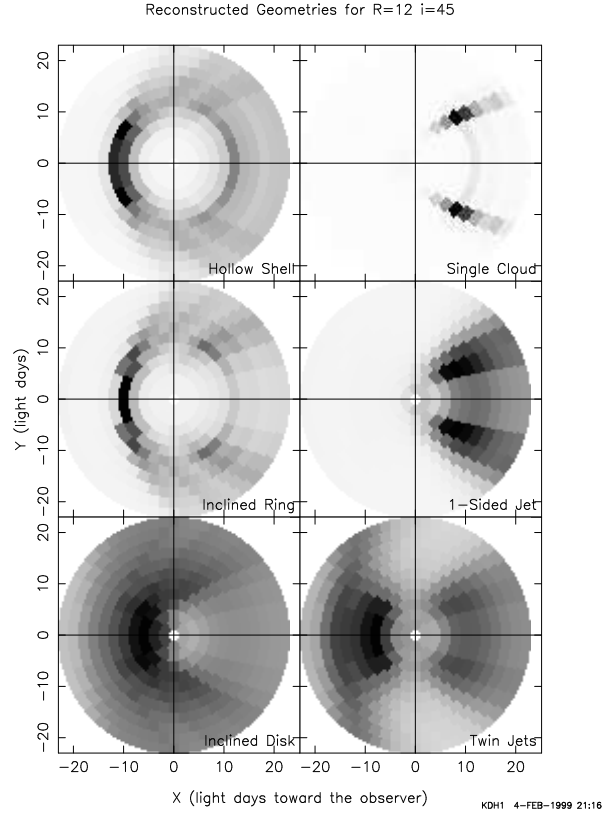


Figure 6. Maps of the six test geometries illustrated in Fig. 1 reconstructed from simulated light curves with time sampling and signal-to-noise levels similar to those shown in Fig. 3.

ical density (e.g. Hamann et al. 2002, see also Fig. 5). This inhibits inward more than outward changes in R .

Motion of clouds along iso-delay parabolas preserves the time-delay constraints imposed by the light curves. On the near side, clouds constrained by τ can move in R with only a little change in θ , while on the far side they can move in θ more than R . This explains why the reconstructed shell in Fig. 4 is sharper on the far side than on the near side. Motion in θ must also be inhibited to some extent by the anisotropic radiation patterns in different lines.

2.3.2 Smooth Maps of Six Geometries

Encouraged by the results obtained for the spherical shell geometry, we decided to more thoroughly test the capabilities of quasar tomography by reconstructing maps from simulated data for a variety of test geometries. Fig. 6 exhibits our reconstructed maps for the six test geometries illustrated in Fig. 1. The maps in Fig. 6 represent the “smoothest” positive maps that fit the data with $\chi^2/N = 1$.

Comparison of Figs. 1 and 6 indicates that significant ambiguities in the geometry remain after imposing constraints from the ultraviolet emission-line light curves. In all six cases the distorted geometry arises because the data constrain U and τ more tightly than n_H , R or θ , as we discussed above in some detail for the hollow shell geometry. While the hollow shell geometry is recognizable in the map, the map of the inclined ring looks quite similar. The map

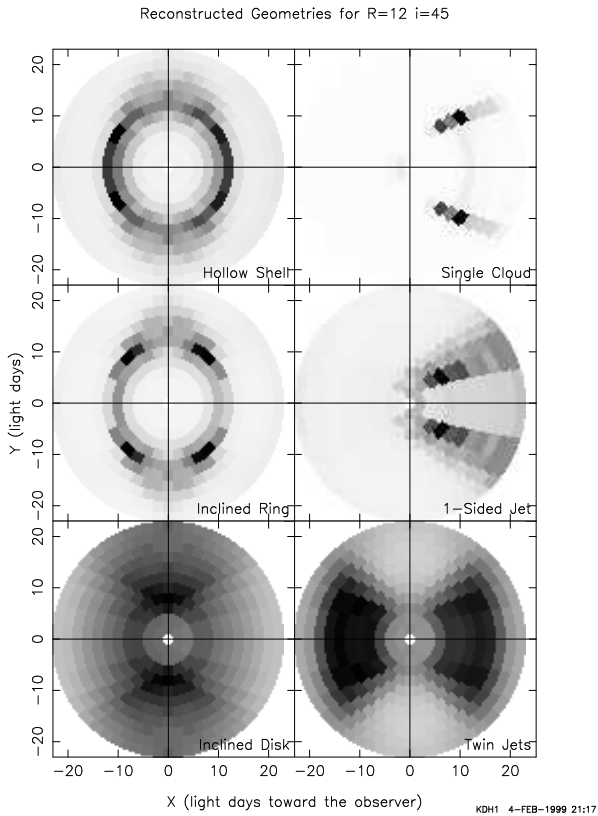


Figure 7. As in Fig. 6 except that here the maps are reconstructed with a preference for front-back symmetry that is characteristic of point-symmetric and axi-symmetric geometries.

of the single cloud is greatly extended along the iso-delay parabola, making it appear similar to the map of the 1-sided jet. The 2-sided jet is hardly recognizable, and the disk is totally unrecognizable, presumably because these geometries extend over large ranges in R , θ , and τ .

The present tests show that the reconstructed geometry can be significantly distorted while still fitting the lightcurves. Nevertheless, we consider that even distorted maps such as these would represent interesting progress given our current limited understanding of the inner regions of active galactic nuclei. Furthermore, ambiguities should decrease as more lines are included in the analysis, since each line responds with a different sensitivity to U and n_H . We also expect to reduce the ambiguity by fitting velocity-resolved rather than velocity-integrated lightcurves, since the line ratio constraints are then available separately for the clouds in each velocity bin, rather than only for the sum of all the clouds. We intend to test these conjectures in future work. We consider next how to make use of prior information on the symmetry of the geometry.

2.3.3 Maps Steered toward Front-Back Symmetry

The maximum entropy mapping formalism (MEM), developed in Appendix B, allows us to incorporate prior information by “steering” the fit toward models that obey some type of symmetry. This is done by defining the entropy in such a way that a local maximum occurs when the model is

symmetric. MEM then selects the model that fits the data with $\chi^2/N = 1$, and is also “simple” in the sense of being “as close as possible” to the desired symmetry.

At present we have relatively little prior information on the distributions and properties of the emission-line clouds in AGNs, though this may change in the future. If we had good reason to assume that the distributions were spherically symmetric, for example, we would be able to make better maps by making use of rather than ignoring that prior information. The maps presented so far are steered toward blurred copies of themselves, so that the only preferred symmetry is a local smoothness. We now consider how to give preference to geometries with specific symmetries.

It may be helpful to think about this “steering” as a way of asking different questions in order to explore a range of maps that are consistent with the data. For example, you may wish to ask “Are the data consistent with a spherical geometry?” MEM delivers an answer to this question in the following way. If there is a spherically-symmetric map that fits the data with $\chi^2/N = 1$, MEM finds that map. Usually there will be many spherical geometries, with different radial profiles, that fit the data. In that case MEM finds the one that is “as smooth as possible” in the radial direction. If no spherical geometries are consistent with the data, MEM finds the map that achieves $\chi^2/N = 1$ and is “as close as possible” to spherical symmetry.

Steering toward spherical symmetry is very appropriate for the hollow shell geometry, and could considerably reduce the distortions we noted in our reconstructed map. However, spherical symmetry is not so appropriate for the other five geometries illustrated in Fig. 1. We therefore opt here for a less restrictive symmetry. As discussed in §2.1, any point-symmetric or axi-symmetric geometry has a map that is symmetric in X , since for each cloud on the near side there is a cloud in the corresponding zone on the far side of the nucleus. We note that four of the six geometries in Fig. 1 are symmetric to rotation about an axis that is inclined to the line of sight. When these axi-symmetric geometries are rotated around the line of sight, the result is symmetric between the near and far side, $f(X, Y) = f(-X, Y)$. We may therefore expect to be able to “improve” our reconstructions of these axi-symmetric geometries by “steering” them toward front-back symmetry. The other two maps, which don’t obey this symmetry, will be altered by this inappropriate steering, but perhaps not by enough to matter.

Fig 7 exhibits the maps that arise when preference is given to maps with front-back symmetry. All six test geometries are now rather more easily recognizable in the reconstructed maps. Smearing is still evident along the parabolic iso-delay surfaces, but this effect is reduced by the front-back symmetrizing in comparison with the results in Fig 6. Be reminded that in all cases the maps fit the data with $\chi^2/N = 1$. Differences among the corresponding maps in Figs. 1, 6 and 7 illustrate ambiguity in the geometry that is permitted by the data. The basic resolution is set by the time delay accuracy, but ambiguity arises primarily because the density is not well pinned down, allowing the cloud distribution to spread in radius along iso-delay parabolas while adjusting the density to hold the ionisation parameter roughly constant. We suspect that this ambiguity can be reduced if the dataset includes additional line fluxes that place tighter constraints on gas densities.

We now briefly discuss each of the maps with a view toward understanding what might be learned about the geometry by interpreting such maps. The best reconstruction is that of the hollow shell, which is quite clearly defined by its map in Fig 7. The tight radial resolution (≈ 2 light days) that was achieved only on the back side of the ring ($-X$) in Fig 6, is now transferred to the front side ($+X$) as well. Outward smearing along time-delay parabolas is reduced and modified by the front-back symmetrizing, leaving the largest radial smearing (≈ 5 light days) near the Y axis. Extrapolating these results, as discussed above, we expect that this hollow shell geometry could be very accurately reconstructed if we steered the model toward spherical symmetry.

The inclined ring should ideally appear as two arcs spanning the Y axis (see Fig. 1). Its map in Fig. 7 is superficially rather similar to that of the hollow shell. The two geometries could probably be distinguished, however, based on the azimuthal distribution of the gas around the ring. In particular, the inclined ring is deficient in clouds near the X axis, and has four bright points at $(X, Y) = (\pm R \sin i, \pm R \cos i)$, corresponding to the nearest and farthest points on the inclined ring. These features are clearly visible in the map and would permit an estimate of the ring inclination. Like the hollow shell map, outward radial smearing is expected and evident where the arcs cross the Y axis.

The inclined disk and twin jet maps in Fig. 7 are closer to their correct geometries, shown in Fig. 1, but are still not very easily recognisable. Both maps do indicate cloud distributions spanning a wide range of radius, in striking contrast to the confined radial range found in the hollow shell and inclined ring maps. The inclined disk map has less gas along the X axis and more along the Y axis, but the disk geometry and inclination are not clearly identifiable. If you were to assume a disk geometry, the map implies an inclination closer to 45° than to 0° (all clouds on Y axis) or 90° (all clouds on X axis).

The twin-jet map has a very clear deficit of gas in a wide zone around the Y axis, with a fairly well defined edge. However, the two jets blend together across the X axis. Somewhat better resolution would be required to infer the correct geometry.

The single cloud and 1-sided jet geometries have clouds exclusively on the near side of the nucleus, with no corresponding clouds on the far side. This violates the preferred front-back symmetry employed in reconstructing the maps in Fig 7. Maximizing the entropy with the preferred symmetry encourages these maps to develop spurious far-side copies of their near-side features. However, it seems that even in these highly asymmetric cases the maps are not much affected, and are quite similar to or perhaps somewhat better than those in Fig 6. The quality of the light curve data constraints must be sufficient in this example to rule out responses at larger time delays, thus over-riding the preferred symmetry.

3 QUASAR DISTANCES

So far we have assumed that the distance of the active galaxy is known. If the distance is incorrect, the assumed luminosity will be incorrect and the resulting maps will be distorted.

How sensitive are the maps to the adopted distance? To put this question the other way, can we use our maps to determine distances and luminosities of active galaxies? If so, then emission-line reverberation studies could provide a new method to measure cosmological parameters such as H_0 and q_0 .

The observed flux from an active nucleus at redshift z is

$$F(\lambda) \equiv \lambda F_\lambda(\lambda) = \frac{L(\lambda_e)}{4\pi D_L^2} = \frac{hc}{\lambda_H} \frac{Q_H S(\lambda_e) \zeta(i)}{4\pi D_L^2}, \quad (10)$$

where $L(\lambda) \equiv \lambda L_\lambda(\lambda)$ is the luminosity, $\lambda_e = \lambda/(1+z)$ is the emitted wavelength,

$$D_L = \frac{cz}{H_0} \left[1 + \frac{(1-q_0)z}{1+q_0z + \sqrt{1+2q_0z}} \right], \quad (11)$$

is the luminosity distance, where H_0 is the Hubble constant and q_0 is the deceleration parameter, Q_H is the emission rate of hydrogen-ionising photons,

$$S(\lambda) = \frac{\lambda_H L(\lambda)}{hc Q_H} = \frac{\lambda_H L(\lambda)}{\int_0^{\lambda_H} L(\lambda) d\lambda} \quad (12)$$

is the dimensionless shape of the photon spectrum, and $\zeta(i)$ is a dimensionless continuum anisotropy factor, allowing the spectrum to depend on the observer's viewing angle i .

As we have seen, by using photoionisation models to fit measured emission-line flux ratios we can in principle constrain the hydrogen density n_H and the ionisation parameter $U = \Phi_H/(n_H c)$, where Φ_H is the hydrogen-ionising flux incident on the emission-line gas. Since $\Phi_H = Q_H/4\pi R^2$, we can estimate the ‘‘photoionisation radius’’

$$R_Q = \left(\frac{Q_H}{4\pi \Phi_H} \right)^{1/2} = D_L \left(\frac{\lambda_H F(\lambda)}{hc \Phi_H S(\lambda) \zeta(i)} \right)^{1/2}. \quad (13)$$

Echo mapping experiments give an independent measurement of the radius, ‘‘reverberation radius’’,

$$R_\tau = \frac{c \tau}{(1+z)(1+\cos\theta)}, \quad (14)$$

which is derived from time delay measurements. Equating R_Q and R_τ then gives the luminosity distance as

$$D_L = \left(\frac{hc \Phi_H S(\lambda_e) \zeta(i)}{\lambda_H F(\lambda)} \right)^{1/2} \frac{c \tau}{(1+z)(1+\cos\theta)}. \quad (15)$$

The Hubble constant (for small z) is then

$$H_0 \approx \frac{cz}{D_L} \approx \left(\frac{\lambda_H F(\lambda)}{hc \Phi_H S(\lambda_e) \zeta(i)} \right)^{1/2} \left(\frac{z(1+\cos\theta)}{\tau} \right). \quad (16)$$

3.1 Distance–Geometry Correlations

Most of the quantities on the right-hand side of the above expressions for D_L and H_0 are constrained by observations: λF_λ and z are directly observed, Φ_H is determined from the emission-line flux ratios, τ is determined from the light curve time delays. The spectral shape $S(\lambda)$ may be estimated from the spectral energy distribution obtained from multi-wavelength observations extending from X-rays to the infrared. The extreme ultraviolet range is not directly observable, and this introduces some uncertainty. Extinction and reddening by dust in the host galaxy and in our own Milky Way must also be taken into account, of course.

The possibility of anisotropic ionising radiation, $\zeta(i) \neq 1$, may be more difficult to diagnose. Unification scenarios suggest that we view Seyfert 1 galaxies near the pole, $i \lesssim 60^\circ$, and Seyfert 2 galaxies at higher inclinations so that a thick dusty torus obscures our view of the broad emission line region. Large equivalent widths of emission lines would imply that the photoionised clouds see a stronger continuum than we do. This effect may be useful in estimating ζ , which appears to be similar in different objects, judging from the similarity of their emission-line equivalent widths.

Ambiguity arises also from $\cos \theta$. We expect $\langle \cos \theta \rangle = 0$ for any point- or axi-symmetric geometry. However, gas could be located preferentially on the far side or near side of the nucleus. Very good light curves may constrain the shape of the time delay map $\Psi(\tau)$, rather than just the mean value of τ , and this would constrain $\cos \theta$. The value of $\cos \theta$ is also constrained by the different anisotropies exhibited by different emission lines. Thus there would appear to be some prospect for constraining $\cos \theta$, although we do not expect this constraint to be very strong unless the data are very good.

Considering the uncertainty in $\cos \theta$, we expect an ambiguity to arise between H_0 and the inferred geometry. A large value of H_0 (or equivalently a lower source luminosity) may be accommodated by decreasing R and increasing $\cos \theta$, i.e. moving gas inward and placing it on the far side of the nucleus. Because $1 + \cos \theta$ can be at most 2, this degree of freedom should allow up to a factor of 2 increase in the inferred value of H_0 . In practice this can only be realised for an extreme geometry with all gas located on the far side of the nucleus. Conversely, a small value of H_0 can be accommodated by increasing R and decreasing $\cos \theta$, thus moving gas toward the observer and out to larger radii so that once again, τ is roughly preserved.

3.2 H_0 from Simulated Data

To investigate prospects for determining H_0 , and to verify the expected correlations outlined above, we performed tests with simulated light curves. We generated fake light curves assuming $H_0 = 60 \text{ km s}^{-1} \text{ Mpc}^{-1}$, and then reconstructed the gas distribution using various values of H_0 to see how that affected the fit to the data and the resulting cloud maps. When we assumed a value of H_0 fairly close to the correct value, it was possible to achieve a good fit to the light curve, as judged by $\chi^2/N = 1$, but with a distorted geometry. When we assumed a very discrepant value of H_0 , it became impossible to achieve $\chi^2/N = 1$. By using the entropy to quantify the distorted geometry, we could identify the correct value of H_0 as that giving the best fit with the simplest geometry.

Representative results are presented in Fig. 8 for a geometrically thin spherical shell geometry, with $R/c = 12$ light days, hydrogen density $n_{\text{H}} = 10^{11} \text{ cm}^{-3}$, and hydrogen column density $N_{\text{H}} = 10^{23} \text{ cm}^{-2}$. The geometry and density maps shown for $H_0 = 40, 60, 90 \text{ km s}^{-1} \text{ Mpc}^{-1}$ are reconstructed by fitting to light curves generated for $H_0 = 60 \text{ km s}^{-1} \text{ Mpc}^{-1}$. In all three cases the fit achieves $\chi^2/N = 1$. The thin-shell geometry is fairly accurately recovered when we assume $H_0 = 60 \text{ km s}^{-1} \text{ Mpc}^{-1}$. For $H_0 = 90 \text{ km s}^{-1} \text{ Mpc}^{-1}$, the map is highly distorted with most of the gas from the shell displaced to smaller R and

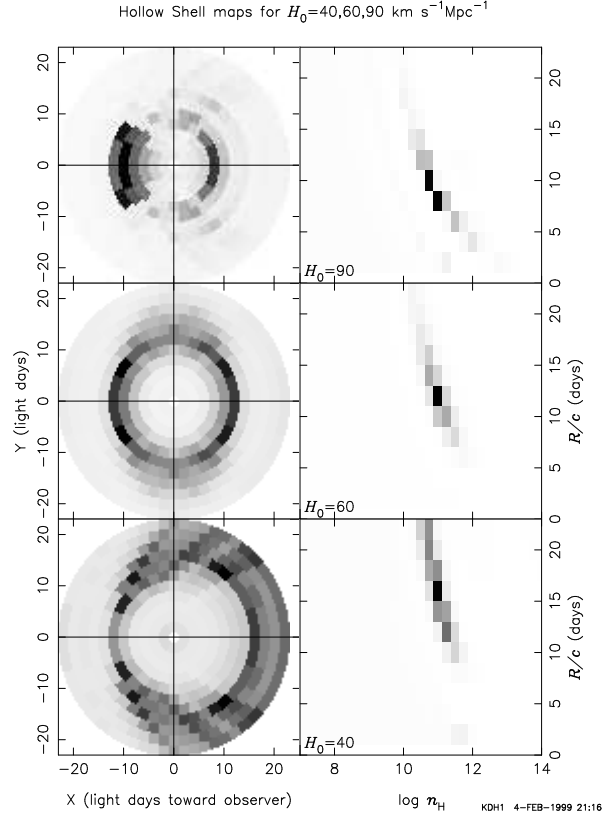


Figure 8. Maps of a spherical shell with $R/c = 12$ d and $n = 10^{11} \text{ cm}^{-3}$ recovered from fits to the simulated data shown in Fig. 3. The Hubble constant used to generate the fake data was $H_0 = 60 \text{ km s}^{-1} \text{ Mpc}^{-1}$, while the three reconstructions assume $H_0 = 40, 60, 90 \text{ km s}^{-1} \text{ Mpc}^{-1}$.

away from the observer to form a clump on the far side of the nucleus. For $H_0 = 40 \text{ km s}^{-1} \text{ Mpc}^{-1}$, the map is distorted in the opposite sense, with gas displaced away from the nucleus and toward the observer along iso-delay parabolas.

The correct value, $H_0 = 60 \text{ km s}^{-1} \text{ Mpc}^{-1}$, may be recognized as the value giving the most symmetric map. The uncertainty in H_0 resulting from such fits may be quantified in terms of the posterior probability distribution derived from the fit

$$P(H_0|\vec{D}) \propto P(\vec{D}|H_0) P(H_0). \quad (17)$$

Here $P(H_0)$ is the prior probability assigned to different values of H_0 before we consider the data \vec{D} . Regardless of our prior view on the value of H_0 , the evidence provided by the data \vec{D} multiplies our prior probability by the factor

$$P(\vec{D}|H_0) \propto \exp \{ \alpha S - \chi^2/2 \}. \quad (18)$$

This applies for each value of H_0 the appropriate penalties for failing to fit the data (large χ^2) and for deploying excessive numbers of parameters (large negative αS , where $S < 0$ is the entropy of the map and $\alpha > 0$ is the mixing parameter). For more detailed discussion, see Appendix B.

4 SUMMARY AND CONCLUDING REMARKS

We have developed a method of reconstructing 5-dimensional maps of photoionised emission-line regions by fitting predictions of photoionisation models to high-quality observations of reverberating emission-line spectra of active galactic nuclei. Reverberation effects in the emission lines offer information about the (R, θ) geometry and the angular emission pattern of the gas clouds, coded as time-delay information in the light curves of different lines with respect to the continuum. At the same time, line profiles give the distribution of clouds with line-of-sight velocity v , line ratios constrain the density n_{H} and column density N_{H} of the gas clouds, and equivalent widths constrain the covering fraction f . Our method brings all these constraints together in a global fit to reverberating emission-line spectra in order to recover a 5-dimensional cloud map, the differential covering factor $f(R, \theta, n_{\text{H}}, N_{\text{H}}, v)$. This method may allow high-quality observations to reveal the geometry, physical conditions, and kinematics of the emission-line gas.

We use the maximum entropy method to find the “simplest” positive maps (maximum entropy) that fit the data ($\chi^2/N = 1$). The entropy is measured with respect to a default map, giving us some freedom to choose what we consider to be a “simple” map. We use the entropy to give preference to smooth maps rather than noisy ones, and to “steer” the map toward various possible symmetries – spherical, axial, point, etc. The range of maps found for different choices of symmetry helps to gauge the extent and nature of ambiguities that remain after fitting the data. The Bayesian formulation provides posterior probability distributions, and Monte Carlo techniques may also be used to assess statistical uncertainties in the cloud map, the distance, and any other parameters that affect the fit.

Tests with simulated datasets indicate good prospects for mapping geometry and density structure from observations of emission-line light curves that show evidence for time delays. Good results require simultaneous fits to numerous lines in order to constrain both the ionisation parameter and the density. The main ambiguity arises because the emission-line lightcurves place tighter constraints on the ionisation parameter U and time delay τ than on the geometry (R, θ) and physical conditions $(N_{\text{H}}, n_{\text{H}})$. Our simulation tests suggest that in some cases the correct geometry is recognizable in the reconstructed maps when we give preference to front-back symmetry, a property of both point-symmetric and axi-symmetric cloud distributions. If geometries are indeed approximately symmetric, then distances can be derived in order to constrain cosmological parameters, $(H_0$ and $q_0)$.

The test cases presented in this paper consider only a single column density, $N_{\text{H}} = 10^{23} \text{cm}^{-2}$. A range of N_{H} at each radius will probably be required to fit observed lightcurves (Shields, Ferland, Peterson 1995). Extending the photoionisation grid to include a range of N_{H} is straightforward, but will require more computer time for the iterative fitting. The additional freedom should also increase the ambiguity, but perhaps not too severely because in general the emission line spectra of clouds in the range $10^{22} < N_{\text{H}} < 10^{24}$ are less sensitive to N_{H} than to U and n_{H} (e.g. Korista et al. 1997; Goad & Koratkar 1998).

We have largely omitted to discuss mapping the kinematics of the emission-line gas, focussing instead on mapping the geometry by fitting to velocity-integrated emission-line light curves. Extracting kinematic information will involve simultaneous fitting of light curves at many wavelengths to resolve time variations and hence time delays at each velocity in the emission-line profile. Extending our analysis to include multiple pixels along the v -axis of the cloud map is straightforward. Note that continuum fitting and de-blending of lines in the observed spectra will not be necessary because the model adds together the predicted continuum and the velocity profiles of all the lines. It will be interesting to see the extent to which $v - R$ projections of $f(R, \theta, n_{\text{H}}, N_{\text{H}}, v)$ provide evidence for virial motions. We expect the use of velocity information to reduce the ambiguities, since constraints will then be available separately for many subsets of the cloud population rather than only for the sum over all clouds.

We rely on CLOUDY both to generate our fake datasets and to reconstruct from them the cloud maps. In the analysis of real observations, uncertainties in the atomic data, in the elemental abundances in the shape of the ionising continuum, and in the assumptions and approximations used in the photoionisation calculations will each give rise to errors and distortions of the maps. It will therefore be important to continue to improve the atomic data and photoionisation physics in tandem with attempts to fit CLOUDY predictions to observations.

Finally, we note that the methods developed here for interpreting spectral variations in active galactic nuclei can also be extended to other types of astronomical objects in which an unknown gas distribution is excited by photoionisation from a compact source of ionising radiation. In cases where time-dependent reverberation effects are not observed, the observed spectrum alone or, better still, spatially-resolved spectral information from combinations of narrow-band imaging and long-slit or integral-field spectroscopy can be used as constraints. Maximum entropy fitting then recovers the “simplest” viable maps of the geometry, kinematics, and physical conditions in the photoionised gas. A likely future application is simultaneous fitting of narrow-band images and long-slit spectra of nova shells and planetary nebulae.

ACKNOWLEDGMENTS

We thank Brad Peterson and Gary Ferland for ideas, inspiration, and helpful comments on the manuscript. PPARC grants supported MRG and KTK at St.Andrews during the period of most rapid progress on this paper. KH acknowledges support from a PPARC Senior Fellowship.

REFERENCES

- Alloin, D., Clavel, J., Peterson, B.M., Reichert, G.A., Stirpe, G.M. 1994, in *Frontiers of Space and Ground-Based Astronomy*, ed. Wamstekar, W., Longair, M.S., Kondo, Y. (Dordrecht: Kluwer), p 423.
- Bahcall, J.N, Kozlovsky, B.Z., Salpeter, E.E., 1972, *ApJ*, 171, 467.
- Baldwin, J., Ferland, G. Korista, K. and Verner, D. 1995, *ApJL*, 455, L119.

- Baldwin, J.A. 1977, ApJ, 214, 679.
 Baldwin, J.A., Burke, W.L., Gaskell, C.M., Wampler, E.J. 1978, Nature, 273, 431.
 Blandford, R.D., McKee, C.F. 1982, ApJ, 255, 419.
 Collier, S., Horne, K., Wanders, I., Peterson, B.M. 1999, MNRAS, 302, 24.
 Clavel, J. et al. 1991, ApJ, 366, 64.
 Davidson, K., Netzer, H. 1979, Rev. Mod. Phys., 51, 715.
 Done, C., Krolik, J.H. 1996, ApJ, 463, 144.
 Edelson, R.A., Krolik, J.H. 1988, ApJ, 333, 646.
 Ferland, G.J., Peterson, B.M., Horne, K., Welsh, W.F., Nahar, S.N. 1992, ApJ, 387, 95.
 Ferland, G.J., Korista, K.T., Verner, D.A., Ferguson, J.W., Kingdon, J.B., Verner, E.M. 1998, PASP, 110, 761.
 Goad, M.R., Koratkar, A.P. 1998, ApJ, 495, 718.
 Goad, M.R., O'Brien, P.T., Gondhalekar, P.M. 1993, MNRAS, 263, 149.
 Gull, S.F. 1989, in Maximum Entropy and Bayesian Methods, ed. Skilling, J., (Dordrecht: Kluwer), p 53.
 Gull, S.F., Skilling, J. 1990, The MemSys5 Users' Manual, Maximum Entropy Data Consultants, Ltd, Royston, UK.
 Hamann, F., Korista, K.T., Ferland, G.J., Warner, C., Baldwin, J. 2002, ApJ, 564, 592.
 Horne, K. 1985, MNRAS, 213, 129.
 Horne, K. 1994, in Reverberation Mapping of the Broad-Line Region in Active Galactic Nuclei. ed. Gondhalekar, P.M., Horne, K., Peterson, B.M. ASP Conference Series Vol 69, p 23.
 Horne, K., Welsh, W.F., Peterson, B.M. 1991, ApJL, 367, L5.
 Kaspi, S., Smith, P.S., Netzer, H., Maoz, D., Januzzi, B.T., Givon, U. 2000, ApJ, 533, 631.
 Kinney, A.L., Rivolo, A.R., Koratkar, A.P. 1990, ApJ, 357, 338.
 Koratkar, A.P., Gaskell, C.M. 1991, ApJS, 75, 719.
 Korista, K.T. et al. 1995, ApJS, 97, 285.
 Korista, K.T., Baldwin, J., Ferland, G.J., Verner, D. 1997, ApJS, 108, 401.
 Krolik, J.H., Horne, K., Kallman, T.R., Malkan, M.A., Edelson, R.A., Kriss, G.A. 1991, ApJ, 371, 541.
 Krolik, J.H., Done, C. 1995, ApJ, 440, 166.
 Marsh, T.R., Horne, K. 1988, MNRAS, 235, 269.
 O'Brien, P.T., Goad, M.R., Gondhalekar, P.M. 1994, MNRAS, 268, 845.
 O'Brien, P.T., Goad, M.R., Gondhalekar, P.M. 1995, MNRAS, 275, 1125.
 Panagia, N., Gilmozzi, R., Macchetto, F., Adorf, H.-M., Kirshner, R.P. 1991, ApJ, 380, 23.
 Pijpers, F.P., Wanders, I. 1994, MNRAS, 271, 183.
 Peterson, B.M. 1993, PASP, 105, 247.
 Reichert, G., et al. 1994, ApJ, 425, 582.
 Shields, J.C., Ferland, G.J., Peterson, B.M. 1995, ApJ, 441, 507.
 Skilling, J., Bryan, R.K. 1984, MNRAS, 211, 111.
 Skilling, J. 1989, in Maximum Entropy and Bayesian Methods, ed. Skilling, J., (Dordrecht: Kluwer), p 45.
 Spruit, H.C. 1994, A&A, 289, 441.
 Ulrich, M.-H., Horne, K. 1996, MNRAS, 283, 748.
 Vio, R., Horne, K., Wamsteker, W. 1994, PASP, 106, 1091.
 Wanders, I., et al. 1995, ApJ, 453, 87.
 White, R.J., Peterson, B.M. 1994, PASP, 106, 879.

APPENDIX A: THE FORWARD PROBLEM

A1 Geometry

Two parameters, Δt and τ_{MAX} , set the pixel size and radius of the region that we wish to map. These need to be chosen appropriately for each dataset. We recommend setting Δt to the median time step between successive data points, and τ_{MAX} to a value larger than the largest delay for which

the data provide evidence of significant response, usually not more than a third of the full duration of the observed light curves. The model includes a constant background spectrum, §A3.1, to allow for responses on larger timescales. Our maximum entropy fits (Appendix B) degrade the resolution of the map as much as possible within the constraints set by the light curve data. If the pixels are too large, the resolution may be limited by the pixel size rather than by the data. If the pixels are too small, the resolution is defined by the data, but more computer time is required to accomplish the fit. Thus high or low signal-to-noise datasets may require smaller or larger Δt , respectively.

A1.1 Shells

In the model developed for this paper, we divide the spatial volume surrounding the nucleus into N_R concentric spherical shells with radii

$$R(i) = i\Delta R, \quad (\text{A1})$$

where $\Delta R = c\Delta t/(1+z)$ and Δt is a suitable time interval comparable to the time spacing of the observations. The time delay range covered by the shells is thus $\tau_{\text{min}} = 0$ to $\tau_{\text{max}} = 2N_R\Delta t$. Any flux arising from outside this region is included in the model in the form of a constant background spectrum (§A3), thus neglecting any reverberation effects. Note that other partitions are possible, for example equal spacing in $\log R$ may be more appropriate if a large range of radius is to be mapped.

The exact choice of Δt is not too critical because in fitting the data we first construct predicted light curves uniformly sampled with a time interval Δt , and then interpolate to the actual times of observations. Given an equally spaced time series, Δt can be the time interval between successive data points. For unequally-sampled time series, Δt can be the minimum or median time spacing, or some point in between. A smaller Δt may permit resolution of finer structure if the data record significant flux changes from one data point to the next. A larger Δt may be adequate if the data record no significant flux changes between successive data points.

A1.2 Zones

The time delay accounting for light travel time is

$$\tau(R, \theta) = \frac{R}{c}(1+z)(1+\cos\theta), \quad (\text{A2})$$

where the angle θ specifies the direction of the gas cloud as seen from the nucleus measured from the direction away from the observer. Note that the time delay depends on θ as well as R , as do the reprocessing efficiencies discussed in §A4 below. We therefore sub-divide shell i into $N_\theta(i) = 2i + 1$ equal-area zones delimited by equal intervals of $\cos\theta$. The solid angle covered by each zone as viewed from the origin is

$$\Delta\Omega = \frac{4\pi}{N_\theta} = \frac{4\pi}{2i+1}. \quad (\text{A3})$$

The cosine of our viewing angle for clouds in zone j of shell i is then

$$\cos\theta = 2\left(\frac{j-1}{N_\theta-1}\right) - 1 = \frac{j-i-1}{i}. \quad (\text{A4})$$

Finally, the time delay is

$$\tau = 2i\Delta t \left(\frac{j-1}{N_\theta - 1} \right) = \Delta t (j-1) . \quad (\text{A5})$$

Note that because we choose $N_\theta = 2i + 1$, the delay spacing is Δt in all shells. The full range of delays is $0 < \tau < \tau_{\text{MAX}} = 2N_R\Delta t$.

Because none of the observable data we consider ^{*} depend upon the angle ϕ measured around the line of sight, we can omit further sub-division of the zones into sectors.

We wish to emphasize that our use of a shell and zone partition of the 3-dimensional volume is completely general and does not exclude any class of models. While we employ nested shells, this does not imply a restriction to a spherically-symmetric geometry, since structure in the angle θ is resolvable by the zones that partition each shell. We do not partition the zones in the angle ϕ , but this does not restrict us to models that are symmetric to rotation around the line of sight. It is just that we are unable to detect any ϕ structure that may exist because there are no aspects of the data that depend upon the angle ϕ . What we can detect, then, is the true 3-dimensional geometry $f(R, \theta, \phi)$ projected by rotation around the line of sight to give a 2-dimensional map

$$f(R, \theta) = \int f(R, \theta, \phi) d\phi . \quad (\text{A6})$$

A1.3 Cloud covering fraction

Zone θ of shell R subtends solid angle $\Delta\Omega$ and contains a population of gas clouds that intercepts a fraction $f(R, \theta) \Delta R \Delta\Omega/4\pi$ of the ionising luminosity. The cloud cover arises from different types of clouds characterized by their hydrogen density n_{H} , column density N_{H} , and line-of-sight velocity component (Doppler shift) v . The cloud geometry is therefore obtained by integrating over the cloud types :

$$f(R, \theta) = \int f(R, \theta, n_{\text{H}}, N_{\text{H}}, v) dn_{\text{H}} dN_{\text{H}} dv . \quad (\text{A7})$$

This introduces the 5-dimensional differential covering fraction map that we aim to reconstruct by fitting to the observed spectral variations. Since f is a distribution, we can use any convenient partition to divide the $(R, \theta, n_{\text{H}}, N_{\text{H}}, v)$ domain. In this paper we employ a partition with equal intervals of R , $\cos\theta$, $\log n_{\text{H}}$, $\log N_{\text{H}}$, and v .

The radial dimension of a cloud of density n_{H} and column N_{H} is $l_R \sim N_{\text{H}}/n_{\text{H}}$. To fit within its spherical shell, the cloud must satisfy $N_{\text{H}}/n_{\text{H}} < \Delta R$. For $\Delta R = 10^{15.4} \text{cm}$ (1 light day), this requires $N_{\text{H}} < 10^{26.4} \text{cm}^{-2} (n_{\text{H}}/10^{11} \text{cm}^{-3})$. In this way we may justify excluding clouds from a corner of the $n_{\text{H}} - N_{\text{H}}$ plane, although our present implementation does not impose this constraint.

If $y > 0$ is a cloud's tangential to radial aspect ratio, we may consider clouds that are spherical ($y = 1$), radially-elongated "cigars" ($y < 1$), or radially-flattened "pancakes" ($y > 1$). The tangential area covered by such a cloud is

$A \sim y^2 (N_{\text{H}}/n_{\text{H}})^2$, and the differential covering fraction for the ensemble of such clouds is then

$$f(R, \theta, n_{\text{H}}, N_{\text{H}}, v) \sim \int y^2 \left(\frac{N_{\text{H}}}{n_{\text{H}}} \right)^2 \frac{\Delta R \Delta\Omega}{4\pi} n_{\text{cl}} dy , \quad (\text{A8})$$

where $n_{\text{cl}}(R, \theta, n_{\text{H}}, N_{\text{H}}, v, y)$ is the volume number density of clouds. Thus our cloud map $f(R, \theta, n_{\text{H}}, N_{\text{H}}, v)$ does not assume spherical clouds but rather represents the combined sky coverage of whatever cloud shapes are present within the volume. Note, however, that in §A4.1 we adopt an anisotropy function that may be more appropriate for spherical clouds than for cigars or pancakes.

A1.4 Cloud shadowing

Our photoionisation code CLOUDY assumes an unobstructed path from the origin out to each cloud. If a cloud is present at position (R, θ, ϕ) , self-consistency demands that clouds at the same θ, ϕ but larger R should be unable to "see" the centre. [†] For our shell-zone geometry, this constraint can be satisfied if

$$f(\theta) = \int_0^{R_{\text{MAX}}} f(R, \theta) \frac{\Delta\Omega \Delta R}{4\pi} \leq 1 . \quad (\text{A9})$$

At present we do not implement this as a hard constraint upon the solution, but rather we use the entropy to "steer" the map toward this constraint (see Appendix B), and check the final result.

A2 Ionising Radiation

We assume that the nucleus is a point source emitting a time-variable spectrum described by

$$L(\lambda, t) \equiv \lambda L_\lambda(\lambda, t) = L_0 S(\lambda) L(t) . \quad (\text{A10})$$

Here the time variations of the nucleus are specified by the dimensionless light curve $L(t)$, the shape of the nuclear spectrum is given by the dimensionless spectrum

$$S(\lambda) = \frac{\lambda_{\text{H}} L(\lambda, t)}{\int_0^{\lambda_{\text{H}}} L(\lambda, t) d\lambda} , \quad (\text{A11})$$

and the dimensional luminosity scale factor is $L_0 = Q_{\text{H}} hc/\lambda_{\text{H}}$, where Q_{H} is the rate at which the nucleus emits hydrogen-ionising photons ($\lambda < \lambda_{\text{H}} = 912\text{\AA}$) in the reference state $L(t) = 1$. This separable form, with $S(\lambda)$ independent of t , assumes spectral shape does not change as the luminosity varies in time. The assumption can obviously be modified if required. The specific shape adopted for the calculations in this paper is shown in Fig A1.

The flux of hydrogen-ionising photons incident on a gas cloud located a distance R from the nucleus is

$$\Phi_{\text{H}}(t) = \frac{Q_{\text{H}} L(t - \tau)}{4\pi R^2} . \quad (\text{A12})$$

[†] The ionising spectrum incident upon the clouds is clearly a combination of the "bare" spectrum from the nucleus together with transmitted, reflected, and diffuse spectral components arising from other clouds. Since fully transparent clouds do not contribute to the overall covering fraction calculation, covering fractions of greater than 1 are possible.

^{*} Polarimetry data might provide a means of resolving structure in ϕ .

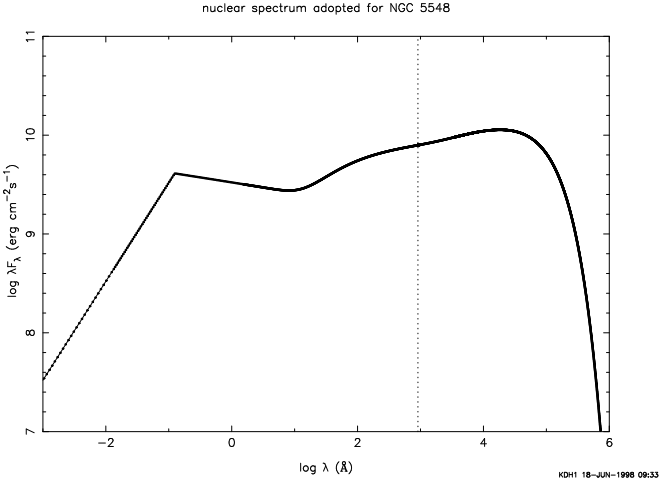


Figure A1. The nuclear spectrum adopted in photoionisation modelling of NGC 5548 and in the simulation tests presented in this paper.

Here t is the time at which we receive the reprocessed photons from the gas cloud, and the time delay τ accounts for the longer light travel time on the path from the nucleus to the gas cloud to the observer compared with the direct path from the nucleus to the observer.

A3 Time-Dependent Spectra

The spectrum that we observe at wavelength λ and time t is modelled as the sum of three components, a time-independent background spectrum, $F_B(\lambda)$, time-variable direct light from the nucleus, $F_D(\lambda, t)$ and reprocessed light, $F_R(\lambda, t)$, arising from gas clouds near the nucleus that are responding to ionising radiation from the nucleus:

$$F(\lambda, t) \equiv \lambda F_\lambda(\lambda, t) = F_B(\lambda) + F_D(\lambda, t) + F_R(\lambda, t). \quad (\text{A13})$$

A3.1 Background Spectrum

The background spectrum $F_B(\lambda)$ is included in the model to account for sources of light that are effectively constant on the timescale spanned by the observed light curves. Such sources include starlight from the host galaxy or nuclear starburst, and reprocessed light from gas outside the domain of the map that respond to the ionising radiation but on timescales much longer than the duration of the light curves.

A3.2 Direct Light

The direct light is

$$F_D(\lambda, t) = F_0 S(\lambda_e) L(t), \quad (\text{A14})$$

where $S(\lambda)$ and $L(t)$ are the dimensionless spectral shape and time variations, and $F_0 = L_0/4\pi D_L^2$ is the dimensional flux observed in the reference state with $L(t) = 1$. Note that with the source at redshift z we must evaluate the spectral shape at the emitted wavelength $\lambda_e = \lambda(1+z)$, and that D_L is the luminosity distance, e.g.

$$D_L = \frac{cz}{H_0} \left[1 + \frac{(1-q_0)z}{1+q_0z + \sqrt{1+2q_0z}} \right], \quad (\text{A15})$$

where H_0 is the Hubble constant and q_0 is the deceleration parameter.

A3.3 Reprocessed Light

The reprocessed light that we see at time t , arises from gas at (R, θ) responding to the ionising flux from the nucleus at the earlier time $t - \tau$, where

$$\tau = \frac{R}{c}(1+z)(1+\cos\theta). \quad (\text{A16})$$

The gas cloud therefore sees an incident hydrogen-ionising photon flux

$$\Phi_H = \frac{Q_H L(t-\tau)}{4\pi R^2}. \quad (\text{A17})$$

We model the spectrum of the reprocessed light as

$$F_R(\lambda, t) = F_0 S(\lambda_0) \int_0^\infty L(t-\tau) \Psi(\tau, \lambda|L) d\tau. \quad (\text{A18})$$

Here $\lambda_0 = 1215\text{\AA}$ is a reference wavelength, discussed in §A4 below. Note that this model accounts for non-linear reprocessing by allowing the delay map $\Psi(\tau, \lambda|L)$ to depend on L , the dimensionless ionising luminosity of the nucleus. Non-linear responses arise because the reprocessing efficiencies of the gas clouds change when they are exposed to different levels of ionising flux. The delay map is obtained by summing contributions from all types of clouds, each contributing at the appropriate delay τ , and weighted by the differential covering fraction f and reprocessing efficiency ϵ :

$$\begin{aligned} \Psi(\tau, \lambda|L) = & \int \frac{d\Omega}{4\pi} dR dn_H dN_H dv \\ & \times f(R, \theta, n_H, N_H, v) \\ & \times \epsilon(\lambda, \Phi_H, n_H, N_H, v, \theta) \\ & \times \delta\left\{\tau - \frac{R}{c}(1+z)(1+\cos\theta)\right\}. \end{aligned} \quad (\text{A19})$$

Here $\epsilon(\lambda, \Phi_H, n_H, N_H, v, \theta)$ is the dimensionless reprocessing efficiency, discussed below, and the Dirac δ function ensures that the correct time delay is used at each reprocessing site.

A4 Reprocessing Efficiencies

The reprocessing efficiencies, ϵ_c for the continuum and ϵ_ℓ for line ℓ , are defined in terms of dimensionless equivalent widths, i.e. the reprocessed flux emerging from the cloud divided by the incident flux λF_λ at the reference wavelength $\lambda_0 = 1215\text{\AA}$. These we evaluate with the photoionisation code CLOUDY (Ferland et al. 1998) for a pre-specified grid in $\log \Phi_H$, $\log n_H$, and $\log N_H$, for given abundances and shape of ionising spectrum (Korista et al. 1997). Linear interpolation in the grid is then used to evaluate the efficiencies as required.

The reprocessed light includes both line and continuum emission:

$$\begin{aligned} \epsilon(\lambda, \Phi_H, n_H, N_H, v, \theta) = & (\lambda_0/\lambda) \epsilon_c(\lambda, \Phi_H, n_H, N_H, \theta) \\ & + \sum_\ell \lambda_0 G_\lambda(x_\ell) \epsilon_\ell(\Phi_H, n_H, N_H, \theta). \end{aligned} \quad (\text{A20})$$

For the reprocessed continuum light, $\epsilon_c(\lambda, \Phi_H, n_H, N_H, \theta)$ gives the ratio of λF_λ for the reprocessed continuum flux divided by that for the incident flux at λ_0 . For the emission

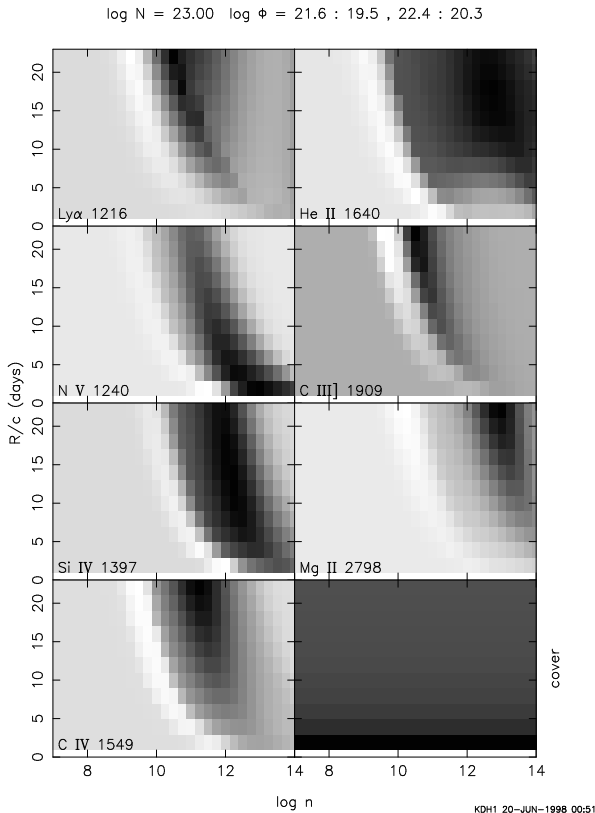


Figure A2. The response as a function of density and radius is shown for each of the major ultraviolet emission lines for a filled spherical volume that reprocesses equal fractions of the ionising spectrum in each unit of radius.

lines $\epsilon_\ell(\Phi_H, n_H, N_H, \theta)$ gives the flux in line ℓ emerging in direction θ divided by the incident flux $\lambda_0 F_\lambda(\lambda_0)$.

When spectra are required, the line emission is assigned a Gaussian distribution in wavelength

$$G_\lambda(x_\ell) = \frac{\exp\{-\frac{1}{2}x_\ell^2\}}{\sqrt{2\pi}\Delta\lambda}, \quad (\text{A21})$$

where

$$x_\ell = \frac{(1+z)\lambda - (1+v/c)\lambda_\ell}{\Delta\lambda} \quad (\text{A22})$$

allows for the Doppler shift by velocity v from the rest wavelength λ_ℓ . The line width $\Delta\lambda$ represents the spectral resolution of the data and intrinsic broadening, e.g., Doppler broadening due to thermal velocities and the range of velocities Δv in the velocity bin.

Fig. A2 examines the responses of the major ultraviolet emission lines to changes in the flux of ionising photons. The figure shows for each radius and density the difference in the line flux between bright and faint states that correspond to an increase by 0.8 in $\log \Phi_H$. In this LOC model, we consider a single column density $\log N_H = 23 \text{ cm}^{-2}$, and a range of densities $7 < \log n_H < 14 \text{ cm}^{-3}$. The radial range considered is $2 < R < 24$ light days, corresponding roughly to a range in the ionising photon flux of $22 > \log \Phi_H > 20$.

Each emission line reprocesses efficiently in a somewhat different region of of the n_H - R plane. The regions are delimited to first order by an appropriate range of the ionisation

parameter $U \propto \Phi_H/n_H \propto Q_H/(R^2 n_H)$. For constant n_H , the reprocessing efficiency diminishes at large Φ_H (small R) because the clouds become fully ionised and heat to Compton temperatures, and at small Φ_H (large R) because only a surface layer on the inward face of the cloud is ionised. Efficient reprocessing requires a higher density at small R , i.e. $n_H \propto Q_H/(R^2 U)$.

In the LOC model, a range of n_H is present at each R , and so the reprocessing regions can simply move outward as the ionising photon flux increases. Clouds on the inner edge of the reprocessing region become less efficient while those on the outer edge become more efficient reprocessors. Lining the inner edge of the reprocessing region is a region of negative response, where increasing the ionising photon flux decreases the reprocessed line flux (see Goad et al. 1993).

At constant U , reprocessing efficiencies decrease at large n_H where collisional processes compete with radiative de-excitation of the upper levels of the transitions. This trend is seen in all lines except N V, whose response increases with increasing n_H . The N V emission line, for solar abundances and the spectral energy distribution assumed here, begins thermalising above $\sim 10^{13} \text{ cm}^{-3}$. If we extended our grid to smaller radius and higher density, the N V emission would decrease again, appearing as C IV does above $\sim 10^{11} \text{ cm}^{-3}$.

A4.1 Anisotropic Emission

The reprocessed radiation is generally emitted with an anisotropic angular distribution, typically because emission is produced on the inward face of an optically thick cloud (Ferland et al. 1992). To allow for anisotropic radiation, the inward efficiency ϵ_I and outward efficiency ϵ_O are computed separately. For the angular pattern of the reprocessed light we assume

$$\epsilon(\theta) = \bar{\epsilon} + (\epsilon_I - \bar{\epsilon}) \cos \theta, \quad (\text{A23})$$

where the mean efficiency is

$$\bar{\epsilon} = (\epsilon_I + \epsilon_O)/2. \quad (\text{A24})$$

The linear dependence on $\cos \theta$ corresponds to isotropic radiation from each point on the surface of a spherical cloud, with the inward and outward fluxes assigned to the inward and outward facing hemispheres.

Fig. A3 shows maps for each of the major ultraviolet emission lines for a filled spherical volume that reprocesses the same fraction of the ionising radiation in each shell. Note that there is a sum over density to obtain the total response in each pixel of the map. The sum over density includes clouds with both positive and negative response. The clouds with positive responses evidently dominate, so that in no part of the emission-line region is there a net negative response.

An inward anisotropy (stronger response from the far side of the map) is evident for most of the lines. This arises from high-density clouds that are optically thick. The exception is C III], which we treated as isotropic in the present calculation. We expect the C III] inward/total ratio to be 0.5-0.6 for clouds that are emissive in this line (O'Brien, Goad & Gondhalekar 1994), and we plan to include this small anisotropy in future calculations.

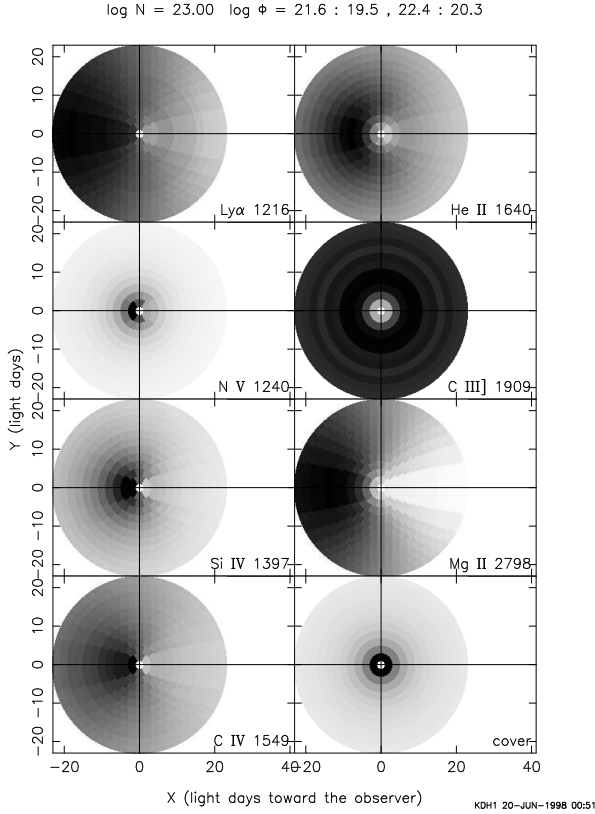


Figure A3. Maps showing the appearance in each of the major ultraviolet emission lines for a filled spherical volume that reprocesses equal fractions of the ionising spectrum in each unit of radius. The inward anisotropy in certain lines is evident.

A5 Delay Maps

Delay maps $\Psi(\tau)$ are shown in Fig. A4. Note that each spherical shell makes a wedge shaped contribution to $\Psi(\tau)$ in the region $0 < \tau < 2R/c$. The near side of each shell contributes at $\tau = 0$ while the far side contributes at $\tau = 2R/c$. The slope of the wedge reflects the degree of anisotropy of the line emission, with steeper slopes indicating increased inward anisotropy. The filled sphere is thus a sum of wedge-shaped contributions from the various shells.

For each emission line the response has been evaluated in both a bright and a faint state, and the corresponding delay maps are shown as solid and dashed curves. Also shown as a dotted curve is the difference between the bright and faint state delay maps, scaled to the same peak value. The dotted curve would be identical to the solid curve if the response is strictly linear, and this is evidently closely satisfied for all of the lines.

The linearity of the responses and the lack of negative responses seen in this LOC model are consistent with the two implicit assumptions normally made when maximum entropy techniques are used to recover delay maps from observed light curves (e.g., Horne, Welsh & Peterson 1991).

A6 Synthetic Light Curves

Fig. A5 shows synthetic light curves calculated for the LOC model. The bottom panel shows the driving light curve,

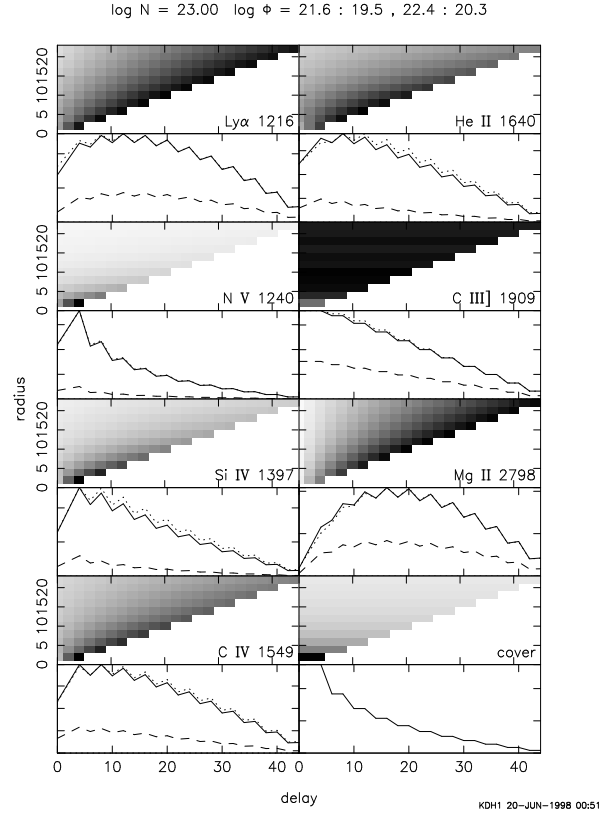


Figure A4. Delay maps for each of the major ultraviolet emission lines for a filled spherical volume that reprocesses equal fractions of the ionising spectrum in each unit of radius. Each shell produces a wedge of emission extending over $0 < \tau < 2R/c$ with a slope that increases with the inward anisotropy.

which was generated assuming that log of the flux executes a random walk in time. The emission-line light curves in the upper panels exhibit variations correlated with those in the driving light curve, but delayed and smeared due to the appropriate delay maps shown to the left of each emission-line light curve.

A7 Synthetic Spectra

Fig. A6 shows synthetic spectra calculated for the LOC model in the bright and faint states. The velocity distribution at each radius is taken to be a Gaussian with dispersion $\Delta v = \sqrt{GM/R}$ for $M = 3 \times 10^7 M_\odot$. The model spectra bear a satisfying resemblance to the observed spectra of Seyfert 1 galaxies, for example NGC 5548 (Clavel et al. 1991). In particular, the C IV/Ly α ratio is close to 1. The main differences are significantly weaker Mg II and C III] emission in the predicted spectrum. From Fig. A3, we see that the Mg II, C III], and Ly α emission regions extend to the 20 light day outer radius assumed in this LOC model. These lines would be stronger if we increased the outer radius.

APPENDIX B: THE INVERSE PROBLEM

Appendix A dealt with the relatively straightforward problem of calculating predicted data $F_\lambda(\lambda, t)$ given a particu-

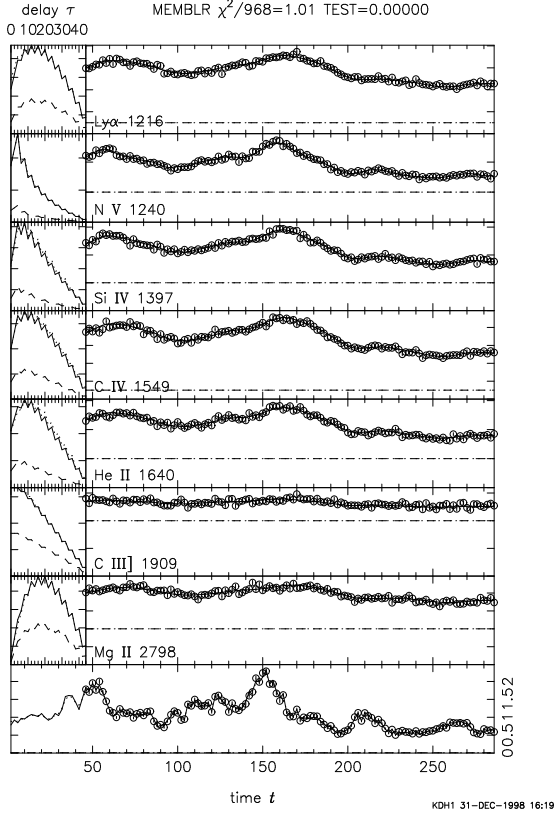


Figure A5. Synthetic light curves for the LOC model.

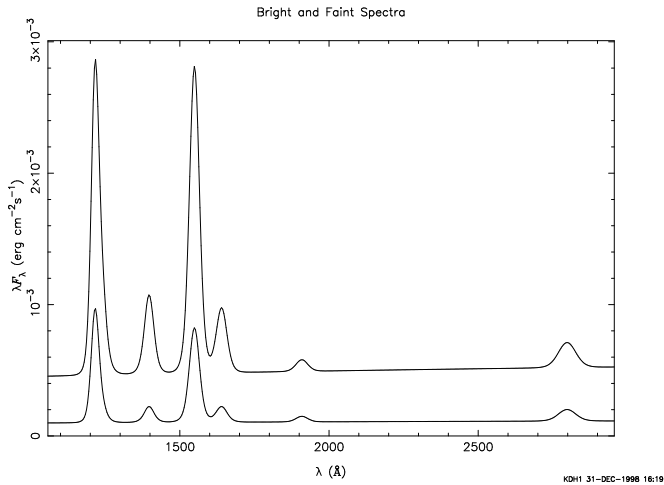


Figure A6. Synthetic bright and faint spectra for the LOC model.

lar cloud map $f(R, \theta, n_H, N_H, v)$. We now tackle the more treacherous inverse of this problem, fitting an observed dataset to recover the underlying cloud map. We accomplish this using maximum entropy fitting methods similar to those we have developed for other astro-tomography problems, for example eclipse mapping (Horne 1985), Doppler tomography

(Marsh & Horne 1988), and echo mapping (Horne, Welsh & Peterson 1991, Horne 1994).

Our discussion of the inverse problem is rather formal because the maximum entropy fitting techniques are based on probability theory and therefore very generally applicable rather than being “ad-hoc” methods limited to our specific problem. Specific examples of maximum entropy fitting applied to the quasar tomography problem are discussed in §2.

We adopt the notation \vec{f} to refer to a vector (or map) of parameters f_i , with i labeling the axes of the parameter space (or the pixels of the map). In quasar tomography, \vec{f} includes several positive additive distributions: the cloud map $f(R, \theta, n_H, N_H, v)$, the light curve $L(t)$, the background spectrum $F_B(\lambda)$, and the distance D . In practice of course we adopt a partition for the domain of each distribution, thereby replacing the infinite-dimensional distribution by a finite-dimensional map \vec{f} .

Constraints on \vec{f} arise from measurements of a data vector \vec{D} , which impose a probability distribution $P(\vec{D})$. In quasar tomography, $P(\vec{D})$ arises from the incomplete and noisy measurements of the time-variable spectrum $F_\lambda(\lambda, t)$. The forward problem, calculating predicted data $\vec{R}(\vec{f})$ given the map \vec{f} , is well defined (Appendix A). The inverse problem, estimating $P(\vec{f})$ given $P(\vec{D})$, is often under-constrained because the number of parameters $M = \dim(\vec{f})$ exceeds the number of data constraints $N = \dim(\vec{D})$. This indeterminacy can be particularly severe when high-quality datasets warrant the use of fine partitions to resolve small structures in the maps.

To cope with the indeterminacy of the inverse problem, we regularize the problem by seeking “the simplest” or “most probable” solutions that fit the observations. This is a good example of “Occam’s razor”: when two models succeed equally well in accounting for the data, the simpler model is more likely to be true.

B1 To Fit the Data: Maximize Likelihood

Bayes’s theorem tells us how to assess the probability of a model with parameters \vec{f} in the light of a dataset \vec{D} . The *posterior probability* of \vec{f} is

$$P(\vec{f}|\vec{D}) = \frac{P(\vec{D}|\vec{f}) P(\vec{f})}{P(\vec{D})}. \quad (\text{B1})$$

Here the *likelihood*, $P(\vec{D}|\vec{f})$, is the probability that \vec{D} arises if we assume that \vec{f} is true. The *prior*, $P(\vec{f})$, is the probability assigned to \vec{f} before \vec{D} was obtained. Finally, the divisor

$$P(\vec{D}) = \int P(\vec{D}|\vec{f}) P(\vec{f}) d\vec{f} \quad (\text{B2})$$

is included to ensure that $P(\vec{f}|\vec{D})$ is a probability density normalized to 1 when integrated over all possible maps \vec{f} .

The likelihood is easy to evaluate. To be specific about the dataset \vec{D} , consider N independent measurements D_i , described by Gaussians with standard deviations σ_i centred on predicted values $R_i(\vec{f})$. The likelihood is then

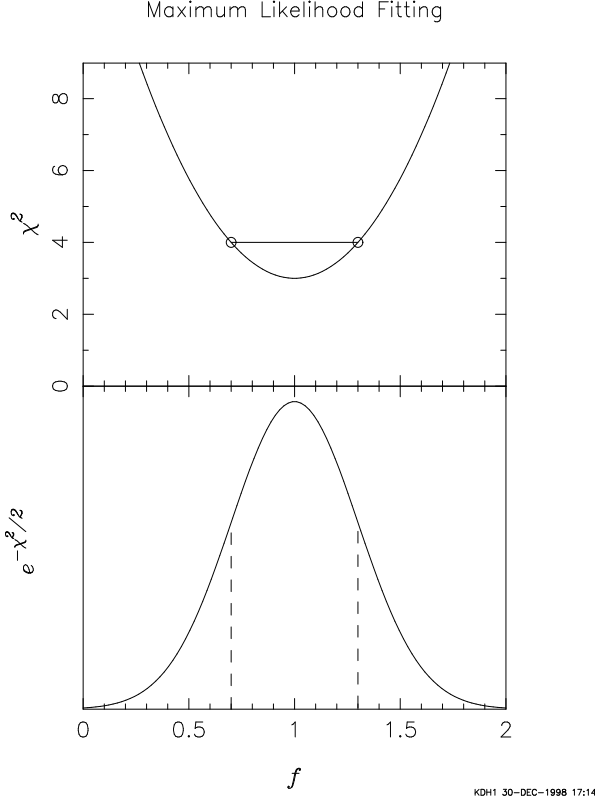


Figure B1. The $\pm\sigma$ confidence interval and the posterior probability distribution are shown for one parameter of a maximum likelihood fit.

$$P(\vec{D}|\vec{f}) = \prod_{i=1}^N P(D_i|\vec{f}) = \frac{\exp\{-\chi^2/2\}}{Z_D}, \quad (\text{B3})$$

where

$$\chi^2 = \sum_{i=1}^N \left(\frac{D_i - R_i(\vec{f})}{\sigma_i} \right)^2, \quad (\text{B4})$$

and the partition function,

$$Z_D = \int \exp\{-\chi^2/2\} d\vec{D} = \prod_{i=1}^N (2\pi\sigma_i^2)^{1/2}, \quad (\text{B5})$$

normalizes the likelihood as a probability density on \vec{D} .

The maximum likelihood method assumes that $P(\vec{f})$ is a uniform distribution. The “best fit” model \hat{f} is the one that maximizes the likelihood. This is equivalent (when σ_i are known) to minimizing χ^2 . A model using M parameters to fit N data points should leave residuals with $N - M$ degrees of freedom. A successful fit should therefore achieve $\chi_{\text{MIN}}^2/(N - M) \approx 1 \pm \sqrt{2/(N - M)}$. The $\pm\sigma$ interval for any parameter of the fit can be found by the criterion $\chi^2 < \chi_{\text{MIN}}^2 + 1$. These concepts are illustrated in Fig. B1.

The Bayesian formulation includes the prior $P(\vec{f})$ to make explicit a fundamental ambiguity involved in the interpretation of data. Different people may use different priors, and thereby arrive at different conclusions from the same data. This is illustrated in Fig. B2.

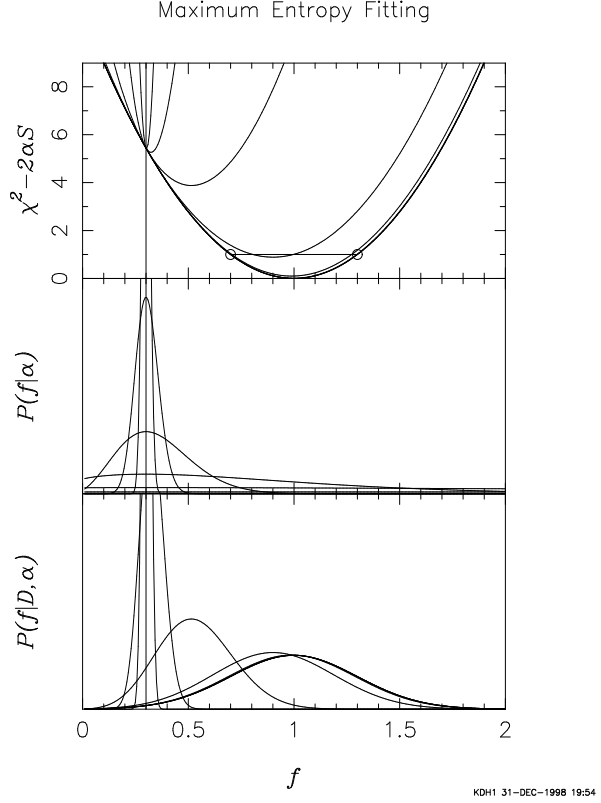


Figure B2. In maximum entropy fitting, we minimize $\chi^2 - 2\alpha S$. The entropic prior $P(f|\alpha) \propto \exp\{\alpha S\}$ peaks at the default value d and has an rms width $(d/\alpha)^{1/2}$. When the regularization parameter α is very small, the prior is so wide that the entropy S is ignored and the posterior probability becomes $P(f|D, \alpha) \propto \exp\{-\chi^2/2\}$. As α increases, the entropy becomes more important. $P(f|D, \alpha)$ then shifts toward the default value and becomes narrower. The optimum value of α is determined in Fig. B3.

B2 For a Simple Map: Maximize Entropy

The maximum entropy method extends maximum likelihood fitting to include models that employ huge numbers of parameters. The entropy quantifies the number of parameters being used in such fits. Maximum entropy fitting seeks the simplest model that fits the data.

In quasar tomography, our M -dimensional parameter vector \vec{f} (equivalently, M -pixel map) arises from partitioning the domains of several *positive additive distributions*, e.g., $f(R, \theta, n_{\text{H}}, N_{\text{H}}, v)$, $L(t)$, $F_B(\lambda)$, and D . If we wish to ensure that our maps take on only positive values, and that our inferences depend on the underlying distributions represented by the maps, and not on specific coordinates or partitions used to slice up the domain of \vec{f} , then the only consistent way to do this (Skilling 1989) is to assign relative probabilities to the various possible maps \vec{f} according to an *entropy* of the form

$$S(\vec{f}) = \sum_{i=1}^M w_i \{f_i - d_i - f_i \ln(f_i/d_i)\}. \quad (\text{B6})$$

Here w_i is a weight proportional to the *volume* of pixel i , and $d_i(\vec{f})$ is the *default value* of f_i .

The entropy is regarded as measuring the “simplicity”

of the map. The simplest map maximizes the entropy, and therefore satisfies

$$0 = \frac{\partial S}{\partial f_i} = -w_i \ln(f_i/d_i) + \sum_{k=1}^M w_k \left(\frac{f_k}{d_k} - 1 \right) \frac{\partial d_k}{\partial f_i}. \quad (\text{B7})$$

Note that the maximum entropy value, $S = 0$, occurs when $f_i = d_i$ for every pixel i . The entropy is an information-like measure of the distance of \vec{f} from its *default map* $\vec{d}(\vec{f})$. Maximizing the entropy “steers” \vec{f} toward \vec{d} , and that is why the d_i are referred to as default values. We discuss in §B7 our prescription for choosing the default map $\vec{d}(\vec{f})$ to make the entropy express a preference for specific symmetries, for example smoothness, or axi-symmetry.

B3 The Entropic Prior

The prior probability associated with the entropy (Skilling 1989) is

$$P(\vec{f}|\alpha) = \prod_{i=1}^M P(f_i|\alpha) = \frac{\exp\{\alpha S(\vec{f})\}}{Z_S(\alpha)}. \quad (\text{B8})$$

This introduces a *regularization parameter*, $\alpha > 0$, and the corresponding partition function,

$$Z_S(\alpha) = \int P(\vec{f}|\alpha) d\vec{f} = \int \exp\{\alpha S(\vec{f})\} d\vec{f}, \quad (\text{B9})$$

which normalizes the entropic prior to a probability density on \vec{f} .

To gain some insight into the meaning of this expression, expand $S(\vec{f})$ in a Taylor series about its peak at $\vec{f} = \vec{d}$, and truncate this to obtain the quadratic approximation

$$S(\vec{f}) \approx \frac{1}{2} \sum_{i,j=1}^M (f_i - d_i) \frac{\partial^2 S(\vec{d})}{\partial f_i \partial f_j} (f_j - d_j). \quad (\text{B10})$$

The corresponding entropic prior is an M -dimensional Gaussian,

$$P(\vec{f}|\alpha) \approx \frac{\exp\left\{\frac{\alpha}{2} \sum_{i,j} (f_i - d_i) \frac{\partial^2 S(\vec{d})}{\partial f_i \partial f_j} (f_j - d_j)\right\}}{Z_S(\alpha)}. \quad (\text{B11})$$

The entropy curvature matrix is given in general by

$$\frac{\partial^2 S(\vec{f})}{\partial f_i \partial f_j} = -\frac{w_i}{f_i} \delta_{ij} + \frac{w_i}{d_i} \frac{\partial d_i}{\partial f_j} + \frac{w_j}{d_j} \frac{\partial d_j}{\partial f_i} + \sum_{k=1}^M w_k \left\{ \left(\frac{f_k}{d_k} - 1 \right) \frac{\partial^2 d_k}{\partial f_i \partial f_j} - \frac{f_k}{d_k^2} \frac{\partial d_k}{\partial f_i} \frac{\partial d_k}{\partial f_j} \right\}. \quad (\text{B12})$$

For our present purposes, specialize to the case of a fixed default map, $\partial d_i / \partial f_j \ll 1$, for which the entropy curvature matrix is diagonal,

$$\frac{\partial^2 S(\vec{f})}{\partial f_i \partial f_j} \approx -\frac{w_i}{f_i} \delta_{ij}. \quad (\text{B13})$$

The entropic prior is then a product of M Gaussian distributions

$$P(\vec{f}|\alpha) \approx \frac{\exp\left\{-\frac{\alpha}{2} \sum_{i=1}^M \frac{w_i}{d_i} (f_i - d_i)^2\right\}}{Z_S(\alpha)}, \quad (\text{B14})$$

with the partition function

$$Z_S(\alpha) \approx \prod_{i=1}^M \left(\frac{2\pi d_i}{\alpha w_i} \right)^{1/2}. \quad (\text{B15})$$

From this we see that the entropic prior admits values in the range $f_i \sim d_i (1 \pm (\alpha w_i d_i)^{-1/2})$. For $\alpha \gg (w_i d_i)^{-1}$, the prior confines attention to a narrow range $f_i \sim d_i$, while for $\alpha \ll (w_i d_i)^{-1}$, a wider range opens to consideration (see Fig. B2). In this way α controls the strength of our prior conviction that the default values d_i are correct. If we wish to set α to a different value for each pixel, this can be done effectively by changing the pixel weights w_i .

B4 The Maximum Entropy Trajectory

Given a dataset \vec{D} , and a regularization parameter α , the posterior probability of our map \vec{f} is

$$P(\vec{f}|\vec{D}, \alpha) = \frac{\exp\{\alpha S - \chi^2/2\}}{Z_Q(\alpha)}, \quad (\text{B16})$$

where the appropriate partition function is

$$Z_Q(\alpha) = \int \exp\{\alpha S - \chi^2/2\} d\vec{f}. \quad (\text{B17})$$

As $\alpha \rightarrow \infty$, the entropy term dominates and the prior becomes so narrow that it over-rides any influence of the data. In the opposite limit, $\alpha \rightarrow 0$, the prior becomes very wide, and we revert to the maximum likelihood fit minimizing χ^2 . Thus α parameterizes a 1-dimensional family of maps $\vec{f}(\alpha)$, the *maximum entropy trajectory* (Gull & Skilling 1990), connecting the maximum likelihood map ($\alpha = 0$), and the maximum entropy map ($\alpha \rightarrow \infty$).

To explore this family of maximum entropy fits, we use the MEMSYS algorithm (Skilling & Bryan 1984) to make iterative adjustments to \vec{f} in order to maximize

$$Q = \alpha S - \chi^2/2. \quad (\text{B18})$$

For any given value of α , the iteration proceeds until the gradients of χ^2 and S are found to be parallel to machine precision, thus assuring that Q is maximized. We begin where we must, with a high value of α , and a simple map that fits the data poorly. We then gradually lower α to reduce the influence of the entropy in comparison with that of the data. For each lower value of α , the map develops additional structure in order to improve the fit. Thus χ^2 decreases monotonically as we pass along the maximum entropy trajectory through progressively lower values of α .

B5 Stopping Criteria

Which value of α should we choose? How strong is our faith that the default values are correct? A justifiable strategy rejects high values of α that produce poor fits to the data, and low values of α that fit the data too well. Based on this motivation, a common practice is to select a value of α that achieves $\chi^2/N = 1$. This is the stopping criterion we have adopted for all the results shown in this paper.

The $\chi^2 = N$ stopping criterion gives a conservative fit. It under-fits the data a bit and omits some of the finer-scale structure in the map. To see this, consider a maximum likelihood fit with M parameters adjusted to fit N data points. The best fit is expected to leave residuals with $N - M$ degrees of freedom, i.e. $\chi^2 \sim (N - M) \pm \sqrt{2(N - M)}$. A fit that achieves $\chi^2 \sim N$ therefore under-fits the data.

A Bayesian stopping criterion aims to maximize the posterior probability of α , given by

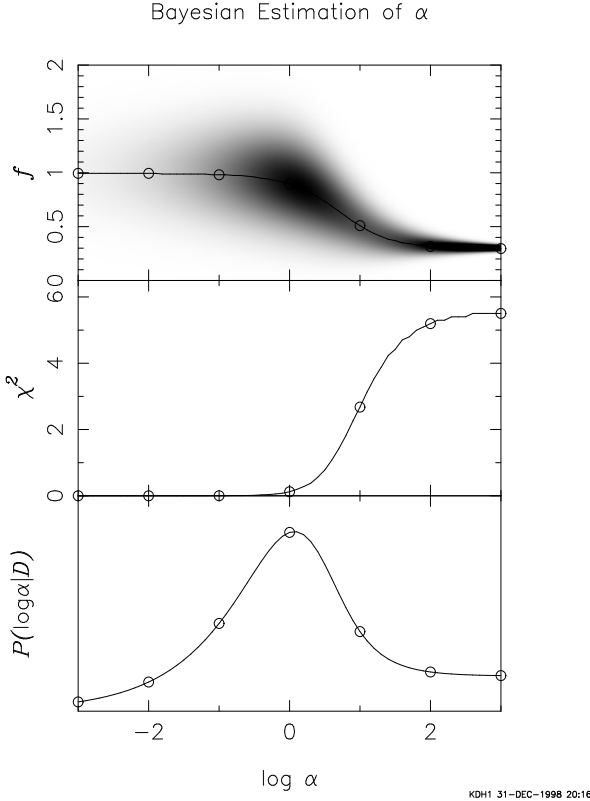


Figure B3. Bayesian determination of the regularization parameter α for the problem illustrated in Fig. B2. If α is large, the entropy pulls the solution to the default value, and the probability is then low because the fit to the data is poor. If α is small, the entropy is ignored. The fit is then good, but the probability is low because there is a penalty for using a very wide prior. The probability peak gives the most likely value of α .

$$\begin{aligned}
 P(\alpha|\vec{D}) &\propto P(\vec{D}|\alpha) P(\alpha) \\
 &= P(\alpha) \int P(\vec{D}|\vec{f}) P(\vec{f}|\alpha) d\vec{f} \\
 &= P(\alpha) \frac{Z_Q(\alpha)}{Z_D Z_S(\alpha)}.
 \end{aligned} \tag{B19}$$

This entails some ambiguity because we are free to choose the prior $P(\alpha)$. Since $\alpha > 0$, a plausible choice is $P(\alpha) \propto \alpha^{-1}$, so that the prior is uniform in $\ln \alpha$. For an example, see Fig. B3.

We expect $P(\alpha|\vec{D})$ to have a maximum at some $\alpha = \hat{\alpha}$, provided $P(\alpha)$ is not too bizarre. To see this, note that for $\alpha \gg \hat{\alpha}$ the emphasis on entropy maximization makes the map very rigid. $P(\alpha|\vec{D})$ will then be small because χ^2 is large – very simple maps fail to achieve good fits to the data. As we decrease α , we move along the maximum entropy trajectory through increasingly flexible maps that develop more structure to improve the fit. For $\alpha \ll \hat{\alpha}$, the map is so flexible that χ^2 approaches an asymptotic minimum value as the fit becomes as good as it can be. In this limit $P(\alpha|\vec{D}) \rightarrow 0$ because $Z_S(\alpha) \propto \alpha^{-M/2}$. The entropic prior is imposing an appropriate penalty (Occam’s razor) on very flexible maps that deploy too many degrees of freedom to achieve their fit. For $\alpha = \hat{\alpha}$ we achieve the best compromise – fitting the data well enough while deploying a minimum number of degrees of freedom in the map.

How many parameters do we employ in a regularized

fit? The map may have an enormous number of pixels – in fact M may be larger than N – so we can’t possibly be using all M degrees of freedom. In fact we are not, because the structure that develops in the map is spatially correlated. Because we are minimizing $\chi^2 - 2\alpha S$, it is plausible to identify $-2\alpha S$ as the effective number of parameters used in the regularized fit. (Note that $-2\alpha S > 0$ because $\alpha > 0$ and $S < 0$.) By analogy with a maximum likelihood fit, then, we should choose α so that $\chi^2 = N + 2\alpha S$. This is only a heuristic justification, but the result can be justified more rigorously (Gull 1989) when the Bayesian stopping criterion is used.

B6 Quantified Uncertainties

The uncertainty of the map \vec{f} after fitting to the data \vec{D} is quantified by its posterior probability distribution. Equation (B16) gives this for each value of α , corresponding to different strengths of faith in the default map.

One can combine these by performing a Bayesian average over α to obtain

$$\begin{aligned}
 P(\vec{f}|\vec{D}) &= \int P(\vec{f}|\vec{D}, \alpha) P(\alpha|\vec{D}) d\alpha \\
 &\propto \int \frac{\exp\{\alpha S - \chi^2/2\}}{Z_D Z_S(\alpha)} P(\alpha) d\alpha.
 \end{aligned} \tag{B20}$$

In many cases, particularly with large numbers of data points and map pixels, the probability peak is narrow enough to permit the use of quadratic approximations to χ^2 and S , yielding an M-dimensional Gaussian probability density centred on the most probable map on the maximum entropy trajectory at $\vec{f}(\hat{\alpha})$.

Inferences about other parameters of the fit, such as the distance, luminosity, and H_0 , may be quantified in the same way,

$$\begin{aligned}
 P(H_0|\vec{D}) &\propto P(\vec{D}|H_0) P(H_0) \\
 &= P(H_0) \int P(\vec{D}|H_0, \vec{f}) P(\vec{f}|\alpha) d\vec{f} P(\alpha) d\alpha \\
 &= P(H_0) \int \frac{\exp\{\alpha S - \chi^2/2\}}{Z_D Z_S(\alpha)} d\vec{f} P(\alpha) d\alpha \\
 &= P(H_0) \int \frac{Z_Q(\alpha)}{Z_D Z_S(\alpha)} P(\alpha) d\alpha.
 \end{aligned} \tag{B21}$$

B7 Default Maps

How shall we choose defaults? We want the entropy to “steer” the solution toward the “simplest” map that fits the data. The default map should therefore be set to whatever we consider to be the simplest map. But what do we consider to be a simple map?

In general, we compute default values as weighted geometric means of “nearby” map values:

$$d_i(\vec{f}) = \exp \left\{ \sum_{j=1}^M B_{ij} \ln f_j \right\}. \tag{B22}$$

Think of the symmetric “blur” matrix B_{ij} as a point-spread function, decreasing with the “distance” between pixels i and j . It is normalized as a probability distribution

$$\sum_{j=1}^M B_{ij} = 1. \tag{B23}$$

This makes $\vec{d}(\vec{f})$ a “blurred” copy of \vec{f} . Each pixel in \vec{f} is then pulled toward its neighbors.

If we set $B_{ij} = 1/M$, then the default map is uniform, and the maximum entropy fit gives the “most uniform” map that fits the data. This would be appropriate when the prior expectation is that no structure is present in \vec{f} . In problems with incomplete data constraints, a uniform default can allow the data to impress bizarre artifacts on the map, for example the ingress-egress arches seen in eclipse maps (Horne 1985).

It is usually more appropriate to seek smooth maps by using “curvature defaults” that steer each pixel value toward the geometric mean of its nearest neighbors,

$$d_i = \sqrt{f_{i+1}f_{i-1}}. \quad (\text{B24})$$

With curvature defaults, the entropy of a 1-dimensional map $f(x)$, partitioned at intervals Δx , approaches a weighted integral of the squared curvature of the logarithm of the map,

$$S \approx - \int \frac{(\Delta x)^4 w(x) f(x)}{2} \left(\frac{\partial^2 \ln f}{\partial x^2} \right)^2. \quad (\text{B25})$$

With constant $w(x)$, this gives preference to $f(x)$ with Gaussian peaks (constant curvature) and exponential tails (zero curvature). With $w(x) \propto x^2$, the solution is steered toward $f(x)$ that are power-laws in x .

In dealing with multi-dimensional maps, for example $f(\vec{x}) = f(R, \theta, n_{\text{H}}, N_{\text{H}}, v)$, there are of course many different curvatures to consider. We compute the default value for pixel \vec{x} by first calculating geometric means of neighbors offset on opposite sides in several chosen directions $\Delta \vec{x}_k$, and then taking a weighted average of those geometric means:

$$\ln d(\vec{x}) = \frac{\sum_k (\Delta_k / \Delta \vec{x}_k)^2 \ln \sqrt{f(\vec{x} + \Delta \vec{x}_k) f(\vec{x} - \Delta \vec{x}_k)}}{\sum_k (\Delta_k / \Delta \vec{x}_k)^2}. \quad (\text{B26})$$

A large Δ_k promotes structures oriented along the direction $\Delta \vec{x}_k$.

We frequently use the default map to steer our solutions toward certain preferred symmetries. For example, to promote a spherical geometry, we would compute defaults by averaging map values over spherical shells. Point-symmetric and axi-symmetric geometries project to maps with front-to-back symmetry, i.e. symmetric on reflection through the Y axis. To promote point- or axi-symmetric geometries, we steer each pixel toward the mean of itself and the pixel with opposite sign of $\cos \theta$. We also apply constraints on the normalization of the map, for example covering fraction must be less than 100%, by imposing the required constraint on the default map. In this way the desired symmetry and normalization are taken on by the map if this is compatible with the data. Otherwise the map comes as close as it can to the desired symmetry and normalization while still fitting the data.

Finally, we note that it may be possible by making a deft choice of default image to suppress to some extent the artefacts that form along the time-delay paraboloids. The strategy would be to first blur the map along the time delay direction, and then mix that in with a negative weight to form the final default image. With negative weight the default will suppress rather than enhance structure in the time-delay direction. This approach has demonstrated some success in suppressing similar artefacts in the eclipse mapping problem (Spruit 1994). A difficulty we see with this approach is in deciding how strongly to apply the negative

weights. We have not attempted to explore this possibility, but may do so in future work.